AD-A174 780 FLUID DYNAMIC - STRUCTURAL INTERACTIONS OF LABYRINTH' 1/1
SEALS(U) MASSACHUSETTS INST OF TECH CAMBRIDGE GAS
TURBINE AND PLASMA D M MARTINEZ-SANCHEZ ET AL
UNCLASSIFIED AUG 86 AFOSR-TR-86-2039 AFOSR-83-0034 F/G 11/2 NL

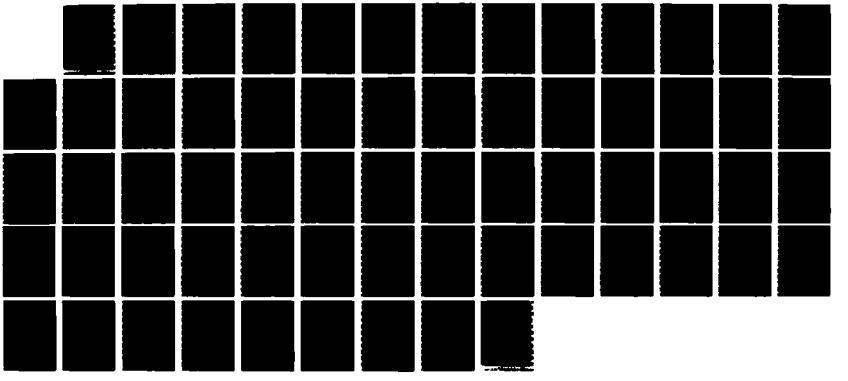

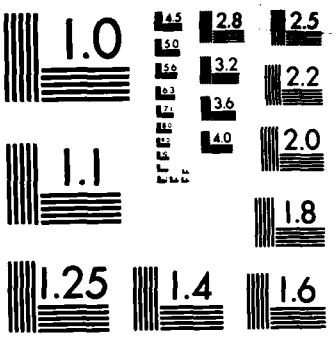

(2)

1

AFOSR-TR- 86-2039

FLUID DYNAMIC - STRUCTURAL INTERACTIONS OF LABYRINTH SEALS

Manuel Martinez-Sanchez

John Dugundji

Gas Turbine and Plasma Dynamics Laboratory

Department of Aeronautics and Astronautics

Massachusetts Institute of Technology

Cambridge, Massachusetts 02139

August 1986

Final Report for Period: 1 December 1983 - 31 December 1984

AFOSR Grant: AFOSR-83-0034

UNCLASSIFIED

SECURITY CLASSIFICATION OF THIS PAGE

(2)

REPORT DOCUMENTATION PAGE

1a. REPORT SECURITY CLASSIFICATION UNCLASSIFIED	1b. RESTRICTIVE MARKINGS
2a. SECURITY CLASSIFICATION AUTHORITY	3. DISTRIBUTION/AVAILABILITY OF REPORT Approved for public release; distribution unlimited.
2b. DECLASSIFICATION/DOWNGRADING SCHEDULE	
4. PERFORMING ORGANIZATION REPORT NUMBER(S)	5. MONITORING ORGANIZATION REPORT NUMBER(S) AFOSR-TR- 86-2039
6a. NAME OF PERFORMING ORGANIZATION Gas Turbine and Plasma Dynamics Laboratory, MIT 6b. OFFICE SYMBOL (If applicable)	7a. NAME OF MONITORING ORGANIZATION AFOSR
6c. ADDRESS (City, State and ZIP Code) MIT, 77 Massachusetts Avenue 47-401 Cambridge, MA 02139	7b. ADDRESS (City, State and ZIP Code) Bolling AFB DC 20332-6448
8a. NAME OF FUNDING/SPONSORING ORGANIZATION AFOSR 8b. OFFICE SYMBOL (If applicable) NA	9. PROCUREMENT INSTRUMENT IDENTIFICATION NUMBER AFOSR 83-0034
8c. ADDRESS (City, State and ZIP Code) Bolling Air Force Base Washington, DC 20332 - 6448	10. SOURCE OF FUNDING NOS. PROGRAM ELEMENT NO.: 61102F PROJECT NO.: 2302 TASK NO.: B1 WORK UNIT NO.:
11. TITLE (Include Security Classification) Fluid Dynamic-Structural Interactions of Labyrinth Seals	
12. PERSONAL AUTHOR(S) M. Martinez-Sanchez and J. Dugundji	
13a. TYPE OF REPORT Final 13b. TIME COVERED FROM 12/1/83 TO 12/31/84	14. DATE OF REPORT (Yr., Mo., Day) August 1986 15. PAGE COUNT 61
16. SUPPLEMENTARY NOTATION	
17. COSATI CODES FIELD / GROUP / SUB. GR.	18. SUBJECT TERMS (Continue on reverse if necessary and identify by block number) Labyrinth Seals, Force Coefficients Rotor Dynamics .

19. ABSTRACT (Continue on reverse if necessary and identify by block number)

Work is described on a continuing investigation into the fluid dynamic and structural interactions of labyrinth seals. Three major areas are considered namely, (a) design and construction of a realistic labyrinth seal test rig to measure stiffness and damping forces in seals, (b) further development of an analytic labyrinth seal test model and its characteristics, and (c) formulation of a structural dynamic rotor system model including labyrinth seal forces and their application to the High Pressure Fuel Turbopump of the Space Shuttle main engine.

20. DISTRIBUTION/AVAILABILITY OF ABSTRACT UNCLASSIFIED/UNLIMITED ☒ SAME AS RPT. ☐ DTIC USERS ☐	21. ABSTRACT SECURITY CLASSIFICATION UNCLASSIFIED
22a. NAME OF RESPONSIBLE INDIVIDUAL ANTHONY K AMOS	22b. TELEPHONE NUMBER (Include Area Code) (202) 767-4937 22c. OFFICE SYMBOL AFOSR/NA

DD FORM 1473, 83 APR EDITION OF 1 JAN 73 IS OBSOLETE.

UNCLASSIFIED

SECURITY CLASSIFICATION OF THIS PAGE

ABSTRACT

Work is described on a continuing investigation into the fluid dynamic and structural interactions of labyrinth seals. Three major areas are considered namely, (a) design and construction of a realistic labyrinth seal test rig to measure stiffness and damping forces in seals, (b) further development of an analytic labyrinth seal test model and its characteristics, and (c) formulation of a structural dynamic rotor system model including labyrinth seal forces and their application to the High Pressure Fuel Turbopump of the Space Shuttle main engine.

FORWARD

This report describes work done at the Gas Turbine and Plasma Dynamics Laboratory (GT&PDL) at the Massachusetts Institute of Technology for the Air Force under Grant No. AFOSR-83-0034. Dr. Anthony K. Amos was the technical monitor.

The work reported herein was performed during the period 1 December 1983 through 31 December 1984. Three graduate students, Otto W.K. Lee, Ya-Pei Chang and Eva Czajkowski worked under the supervision of Professors Manuel Martinez-Sanchez and John Dugundji at some time during this period.

1. INTRODUCTION

As explained in the previous Yearly Report, the purpose of this program was to extend our knowledge of the fluid forces arising from the presence of labyrinth seals in high power turbomachinery, and to relate these forces to their dynamical effects on the turbomachine structure. Thus, the investigation was divided into two parts, one dealing with the fluid aspects and the other with the structural dynamics part of the problem. This report will detail our progress in each of these two areas during the second year of our Grant.

2. WORK PERFORMED

2.1 Fluid Dynamics of Seals.

(a) Test Facility

In previous the Yearly Report (Ref. 1) we described the formulation of an analytical model of the fluid mechanics of a multi-chamber labyrinth which operates in the presence of shaft whirling motion. A preprint which was later presented (Ref. 2) at the 3rd Workshop on Rotor Dynamic Instability Problems in High Performance Turbomachinery (Texas A&M University, May 28-30, 1984), was included as an Appendix.

One of the important points that came out of this work was the fact that theory predicts seal whirl-dependent (damping) forces of the same order as the static (stiffness) forces, and yet no experimental data were available for validation. This has led us to undertake the design of a seal test rig in which the rotor will have both spin and

whirl motion, and these will be controllable. Since theory also indicates that non-pressure forces are secondary, measurements will be made of the time-dependent non-uniform pressure pattern, to yield cross-forces by integration.

In addition to the ability to produce controllable spin and whirl, the requirements on this test rig include (a) Realistic pressure drops, i.e., a pressure ratio of 1.3 in the last seal strip. (b) Constriction Reynolds no. of at least $1\text{-}2\times10^4$ to prevent unwanted low R_e effects. (c) Linear rotor speeds comparable with the axial gap flow velocity, i.e., of the order of 100 m/sec. (d) Provision for controllable inlet flow swirl with tangential velocities of the same order as the rotor speed, or the axial gap velocity. Secondary specifications include modularity (i.e., a capability to include various types of seals and seal lands, as well as a range of number of glands per seal), a reasonably large nominal gap (to allow precise setting of the eccentricity) and solid construction to minimize vibrations.

The test section will operate in air, discharging into the room. For steady operation we will directly connect to an existing Gas Turbine Laboratory oil-free air compressor (0.3 kg/sec, 6 atm). For tests requiring higher flow we can operate in a blow-down mode using the 60 m^3 of pressurized air (6 atm) available. For example, for 4 atm inlet pressure, a 20 sec blow-down will only vary inlet conditions by about 5%. Table 1 lists several test conditions achievable with this rig:

TABLE 1 Test Conditions for Seals Test Rig

N (No. of strips)	P_o/P_e (Press. ratio)	P_o (atm)	δ Nominal gap (mm.)	$\dot{m}$ (Kg/sec)	R_{e_x} Axial gap R_e No.	Operating Mode
2	1.54	1.54	0.6	0.127	15,000	Steady
2	1.54	1.54	0.8	0.169	20,000	Steady
2	1.54	1.54	1.2	0.254	30,000	Blow-Down
20	3.85	3.85	0.6	0.127	15,000	Steady
20	3.85	3.85	0.8	0.169	20,000	Steady
20	3.85	3.85	1.2	0.254	30,000	Blow-Down

A conceptual design including a set of nested eccentric bearings for whirl generation was included in our Proposal for renewal of this Grant. That design has since evolved, although retaining the same operating principles. Fig. 1 shows our current preliminary design. The spinning shaft is supported by a set of inner bearings, whose outer race rests on an eccentric insert. This insert is housed on the inside of an intermediate cylinder, which can itself spin concentrically on a set of outer bearings supported by the outer casing. The intermediate cylinder rotation is provided by a separately driven pulley. This arrangement forces the geometrical axis of the shaft to execute a small satelliting motion about the casing center, at the frequency of the intermediate cylinder rotation. Superimposed on this whirl, there is the shaft spin, driven through a flexible connector that can accomodate

the small parallel translations of the shaft. The linear speed of 100 m/sec at the test seal requires, with the 30 cm diameter, a spin of 6370 RPM. Since whirl occurs typically at 1/2 the shaft rotational speed, we plan to provide belt drive speeds up to 3180 RPM.

The air supply head is structurally separated from the rotating assembly casing, to minimize vibration and stress transmission. The rotating assembly is supported on a single ring flange for the same reasons. A dummy disc is mounted on the shaft end opposite the test seal disk to provide mass symmetry. To reduce vibratory loads due to the eccentricity of the shaft, we will add counterweights attached at appropriate sites on the outer surface of the intermediate cylinder.

Air is supplied to the test seal inlet by two different routes, one arranged to feed concentrically the seal inlet annular plenum, the other arranged to provide tangential momentum to that plenum. By varying the relative feed rates, inlet swirl can be controlled over a wide range. High pressure air is also diverted to the back side of the test seal disk in order to provide at least partial thrust balancing.

The seal land is a separately mounted ring which can easily be interchanged (as can the test seal itself). The primary instrumentation will consist of two or more high response, flush mounted, pressure transducers per seal chamber. To increase sensitivity, these transducers will be referenced to a ring manifold kept at the average chamber pressure by means of a number of small orifices distributed over the seal's periphery and connecting to the manifold. Additional instrumentation will include precise displacement

transducers and case-mounted accelerometers, plus whirl and spin tachometers, and flow meters.

(b) Analytical Studies

The work presented in the Appendix to our previous yearly report has been substantially extended by a careful examination of the physical mechanisms responsible for the computed seal forces. This was accomplished by non-dimensionalizing the governing linearized equations and comparing the relative magnitudes of the various terms. We could thus identify two primary fluid effects as being responsible for the bulk of the cross-forces: (a) Unsymmetric tangential momentum addition to each chamber when the flow swirl varies axially in the presence of shaft offset and (b) Azimuthal variations of flow area within each chamber due to the offset. Both of these induce pressure non-uniformities that integrate to yield cross-forces. The direct contribution of shear forces is shown to be small, but friction does play an important role in generating the flow swirl changes that lead to effect (a) above. The Alford passage-contraction effect is seen to contribute only to direct stiffness, and is thus of only minor importance to stability.

The revised version of our 1984 paper (Ref. 2), containing the analysis that leads to the above conclusions, is included as Appendix A to this Report. This paper is being submitted for publication in the ASME Journal of Engineering for Gas Turbines and Power. The initial formulation and the numerical results (about 50% of the paper) is

identical with Ref. 2.

Also completed during this work period and listed as Ref. 3 is the Master's Thesis by Otto. W.K. Lee, which contains the development and initial numerical results of the linearized theory. This was submitted in Feb. of 1984. The code was later refined and the computations repeated by a new graduate student, Eva Czajskowski, who also performed supporting experimental studies on the details of the intra-cavity pressure distribution in a seal. This work will be reported in our next Yearly Report.

2.2 Structual Dynamics

A structural dynamic model of rotating turbomachinery has been developed to study the effects of labyrinth seal forces on dynamic stability. The model consisted of a flexible rotor with bearings and labyrinth seals mounted on a rigid or flexible case. In addition to the conventional "stiffness" and "damping" expressions, additional "mass inertia" and "dynamic memory" effects are used to represent the labyrinth seal forces. These additional expressions were obtained by fitting the conventional frequency dependent stiffness and damping terms with Padé approximants, to give frequency independent (constant coefficient) stiffness, damping, mass and lag terms which can then be used in a traditional eigenvalue analysis to examine possible rotordynamic instabilities.

The above rotordynamic formulation was developed in a Master's thesis by Y.P. Chang (Ref. 4), and applied to the High Pressure Fuel Turbopump (HPFTP) of the Space Shuttle main engine. Preliminary results indicated that the labyrinth seal forces induce instability, but this instability can be delayed by increasing bearing direct damping.

In the analysis of Ref. 4, the rotor was modeled as a rotating free-free beam, with rigid body translations q_y, q_z and rotations θ_y, θ_z as shown in Fig. 2. The bending deflections W, V of the rotor were first described with reference to a rotating frame, and later transformed to a fixed frame. The rotor was interconnected to a rigid or flexible case at the bearings and at the labyrinth seals by

appropriate spring, damping, and seal forces. Figure 3 shows the dynamic model of the High Pressure Fuel Turbopump (HPFTP) rotor used for the analysis with the associated bearing and seal locations. This rotor model as well as a model of the surrounding case, are given by Muller (Ref. 5), together with the appropriate dynamic properties.

The labyrinth seal forces for the impeller seals 1,2,3 were estimated using the theory developed earlier by Lee, Martinez-Sanchez and Czajkowski (Ref. 2). In this theory, the forces in the y and z directions are given as

$$F_y = -k_{yy}y - b_{yy}\dot{y} - k_{zy}z - b_{zy}\dot{z}$$

$$F_z = k_{zy}y + b_{zy}\dot{y} - k_{yy}z - b_{yy}\dot{z} \qquad (1)$$

where circular symmetric motion of a symmetric shaft has been assumed. The conventional spring and damping coefficients k_{yy}, k_{zy}, b_{yy}, b_{zy} are dependent on the whirl frequency ω as well as the rotation frequency Ω. Since the whirl frequency ω is generally to be determined from the roots of the resulting stability analysis, an iteration process must be done to match the roots with the ω assumed for the seal force coefficients. To avoid this iteration, the seal force coefficients were fitted by Padé approximants over a wide range of whirl frequencies ω, as is often done in aircraft aeroelastic calculations (Ref. 6). The resulting seal forces of Eq. (1) were then alternately expressed as,

$$F_{1y} = -k_{1yy} - b_{1yy}\dot{y} - m_{1yy}\ddot{y} - G_{01}\int_0^t e^{-g_{01}(t-\tau)}\dot{y}(\tau)d\tau$$
$$+ k_{1zy}z + b_{1zy}\dot{z} + m_{1zy}\ddot{z} + G_{03}\int_0^t e^{-g_{03}(t-\tau)}\dot{z}(\tau)d\tau$$
$$F_{1z} = -k_{1zy}y - b_{1zy}\dot{y} - m_{1zy}\ddot{y} - G_{03}\int_0^t e^{-g_{03}(t-\tau)}\dot{y}(\tau)d\tau$$
$$- k_{1yy}z - b_{1yy}\dot{z} - m_{1yy}\ddot{z} - G_{01}\int_0^t e^{-g_{01}(t-\tau)}\dot{z}(\tau)d\tau \qquad (2)$$

where all coefficients are now independent of whirl frequency ω, and additional "mass" and "lag" terms appear in addition to the conventional stiffness and damping terms. Figure 4 shows a typical example of the 2nd impeller seal coefficients k_{yy}, b_{yy}, ...and their variation with whirl frequency ω at the rotational speed Ω = 3708 rad/sec, along with the appropriate Padé fit by the whirl frequency independent coefficients k_{1yy}, b_{1yy},.....

The whirl frequency independent seal forces of Eq. (2) were combined with the structural dynamic analysis to form a conventional linear system of constant coefficient equations of the form,

$$\underset{\sim}{M}\,\ddot{\underset{\sim}{q}} + \underset{\sim}{B}\,\dot{\underset{\sim}{q}} + \underset{\sim}{K}\,\underset{\sim}{q} + \underset{\sim}{G}\,\underset{\sim}{W} = \underset{\sim}{F}(t)$$
$$\underset{\sim}{N}\,\dot{\underset{\sim}{w}} + \underset{\sim}{H}\,\underset{\sim}{w} = -\underset{\sim}{R}\,\underset{\sim}{q} \qquad (3)$$

where $\underset{\sim}{q}$ represents the structural degrees of freedom, and $\underset{\sim}{w}$ are augmented state variables defined by,

$$w_i(t) = \int_0^t e^{-g_{0i}(t-\tau)} \dot{q}_i(\tau)\,d\tau \qquad (4)$$

To examine Eqs.(3) for stability, the forcing terms $\underset{\sim}{F}(t)$ were set to zero, and the equations were rewritten in first order form as,

$$\dot{\underset{\sim}{X}} = \underset{\sim}{A}\,\underset{\sim}{X} \qquad (5)$$

where,

$$A = \begin{bmatrix} 0 & \underset{\sim}{I} & 0 \\ -\underset{\sim}{M}^{-1}\underset{\sim}{K} & -\underset{\sim}{M}^{-1}\underset{\sim}{B} & -\underset{\sim}{M}^{-1}\underset{\sim}{G} \\ 0 & \underset{\sim}{N}^{-1}\underset{\sim}{R} & -\underset{\sim}{N}^{-1}\underset{\sim}{H} \end{bmatrix} \quad , \quad \underset{\sim}{X} = \begin{bmatrix} \underset{\sim}{q} \\ \dot{\underset{\sim}{q}} \\ \underset{\sim}{w} \end{bmatrix}$$

Assuming homogeneous solutions $\underset{\sim}{X}(t) = \underset{\sim}{X}e^{pt}$ led to a standard eigenvalue problem for the roots p, which was solved at each rotational speed Ω. Any positive root or root with a positive real part indicated instability.

Figure 5 shows a root locus plot of the roots p for the rotor mounted on a rigid case. Instability is seen to occur at a rotation speed below Ω = 1000 rad/sec and with a whirl frequency ω = 2100 rad/sec. The addition of some bearing damping is seen to stabilize the system somewhat. Figure 6 shows the corresponding roots for the rotor on a flexible case. The numerical results for these analyses seem to show some minor discrpancies and discontinuities, which will be examined further in a subsequent report by another graduate student.

3. ACCOMPLISHMENTS

1. A labyrinth seals test rig has been designed, and is currently being constructed. The test rig will provide realistic pressure drops and Reynolds numbers, and will attempt to measure both stiffness and damping forces for various whirl and rotation frequencies.

2. An analytic model has been developed for labyrinth seal forces in turbomachinery. A Master's Thesis based on this work has been written by Lee (Ref. 3) and a paper was presented to the 3rd Workshop on Rotor Dynamic Instability Problems in High Performance Turbomachinery (Ref. 2). Subsequent extension of this work including non dimensionalization of the resulting equations has revealed the importance of unsymmetrical tangential momentum addition to each chamber, and azimuthal variations of flow area within each chamber due to shaft offset. A paper based on this work is being submitted for publication to the ASME Journal of Engineering for Gas Turbines and Power, and is included as Appendix A of the present report.

3. A structural dynamic stability formulation has been developed for a rotor system using the labyrinth seal forces developed earlier for the seals. The whirl frequency dependent seal forces were reformulated using Padé approximants as frequency independent stiffness, damping, mass and lag coefficients which can then be used in a traditional eigenvalue analysis to examine possible rotor dynamic instabilities. The dynamic stability formulation was applied to the High Pressure Fuel

Turbopump of the Space Shuttle main engine. Further details of this work are given in a Master's thesis by Chang (Ref. 4).

REFERENCES

1. Martinez-Sanchez, M. and Dugundji, J., "Fluid Dynamic - Structural Interactions of Labyrinth Seals", Final Report on AFOSR Grant AFOSR-83-0034 for the period: 1 Dec. 1982 - 30 Nov. 1983.

2. Lee, O.W.K., Martinez-Sanchez, M. and Czajkowski, E., "The Prediction of Force Coefficients for Labyrinth Seals", Proceedings of the III Workshop on Rotor Dynamic Instability Problems in High Performance Turbomachinery", Texas A&M University, May 28-30, 1984.

3. Lee, Otto W.K., "Prediction of Aerodynamic Force Coefficients in Labyrinth Seals", M.S. Thesis, M.I.T., Dept of Aeronautics and Astronautics, February 1984.

4. Chang, Ya-Pei, "Structural Dynamics of Rotating Turbomachinery with Labyrinth Seal Effects", M.S. Thesis, M.I.T., Dept of Aeronautics and Astronautics, August 1984.

5. Muller, G.R., "Finite Element Models of the Space Shuttle Main Engine", NASA TM-78260, NASA Marshall Space Flight Center, Alabama, January 1980.

6. Edwards, J.W., Ashley, H., Breakwell, J.V., "Unsteady Aerodynamic Modeling for Arbitrary Motions", AIAA Journal, Vol. 17, April 1979, pp. 365-374.

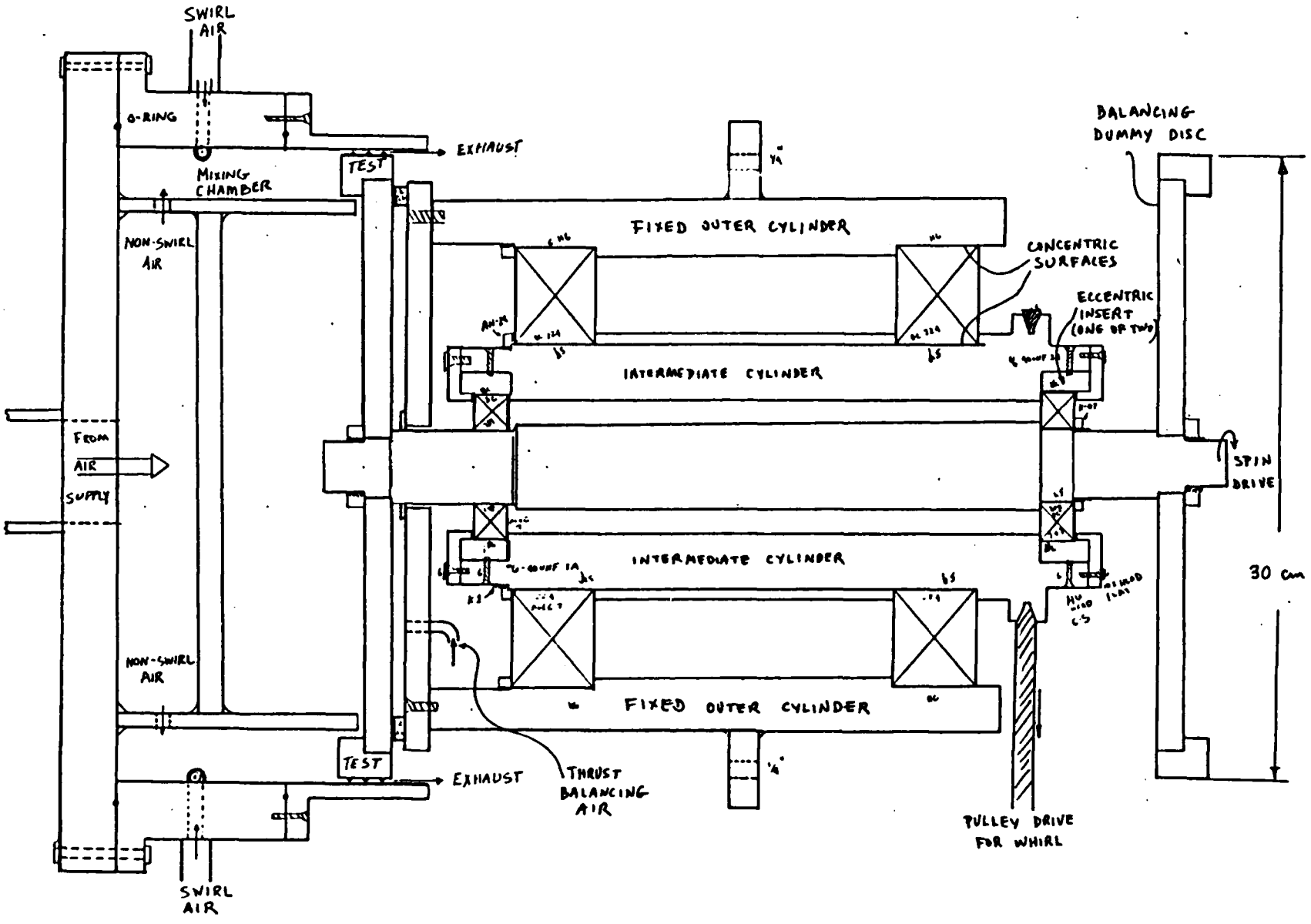

Fig. 1 Preliminary Seals Test Rig Design

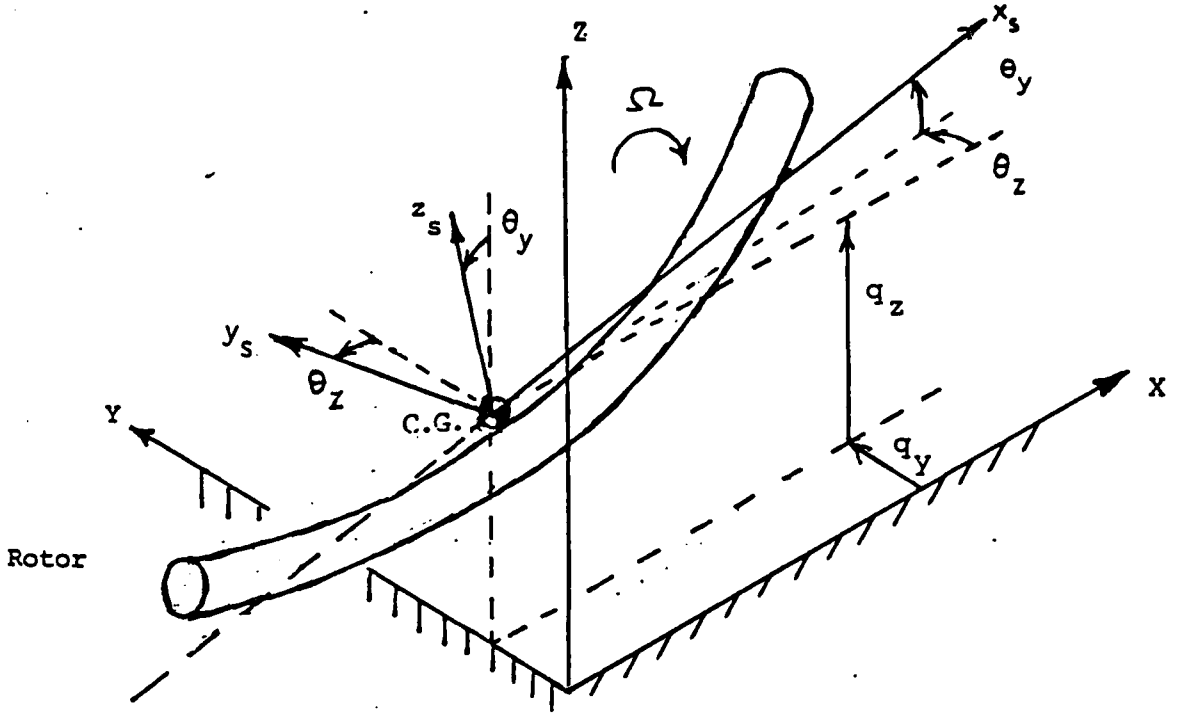

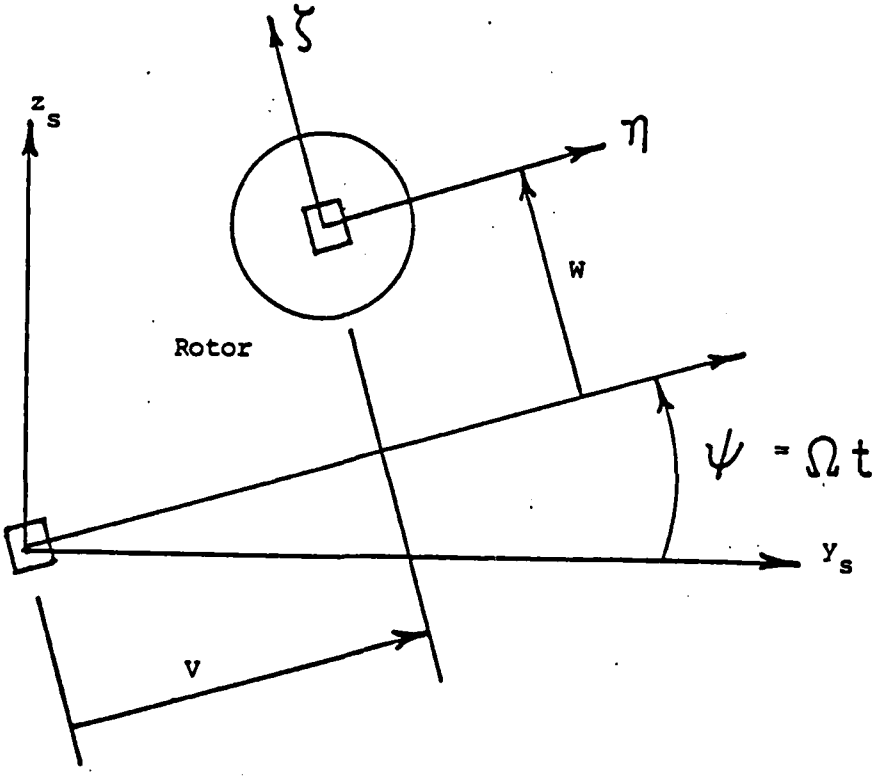

Fig. 2 Rotor Model Axes and Coordinates

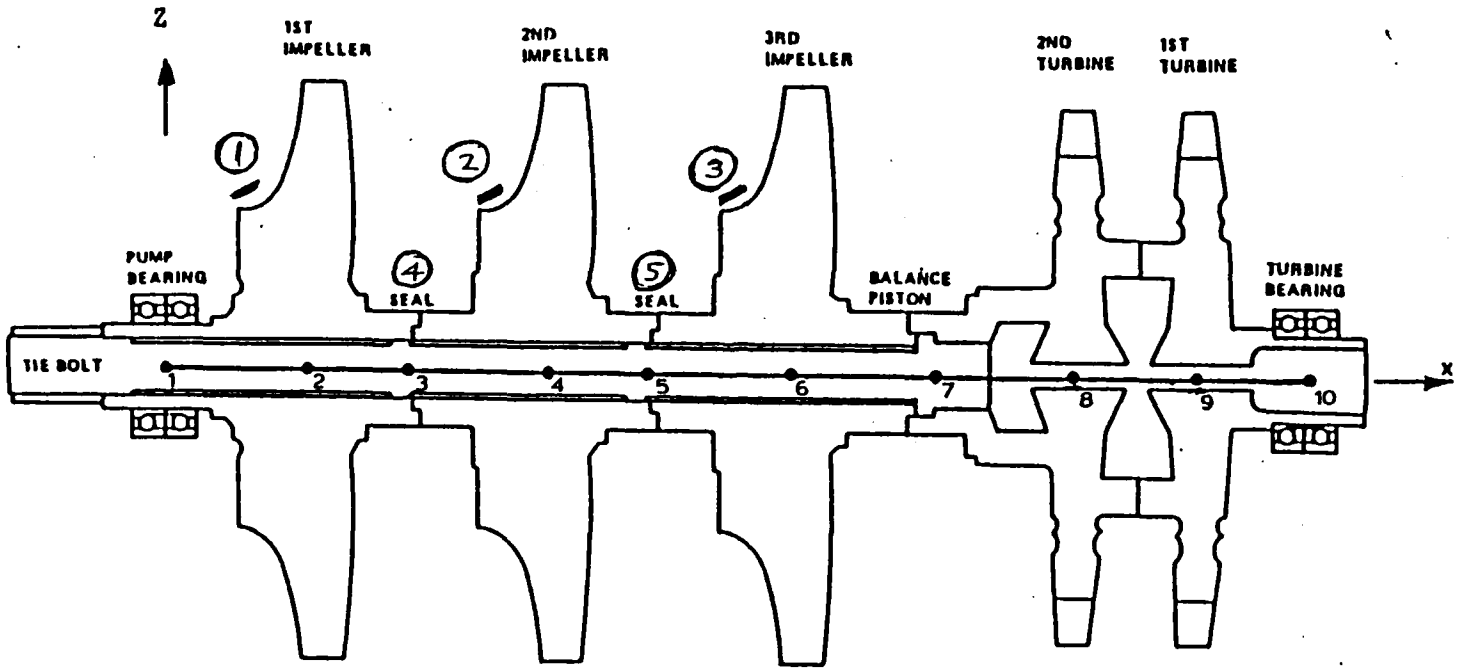

Fig. 3 High Pressure Fuel Turbopump (HPFTP) Rotor Model

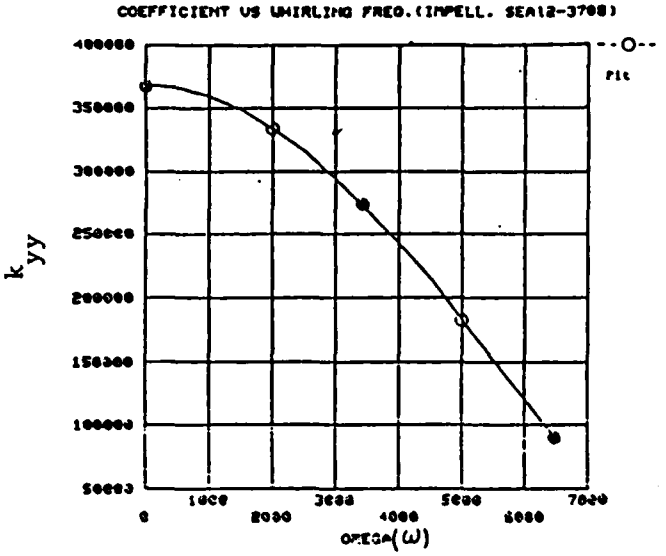

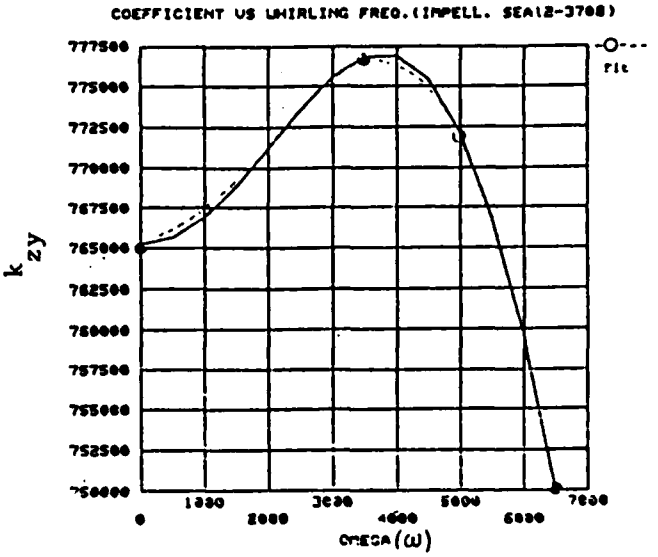

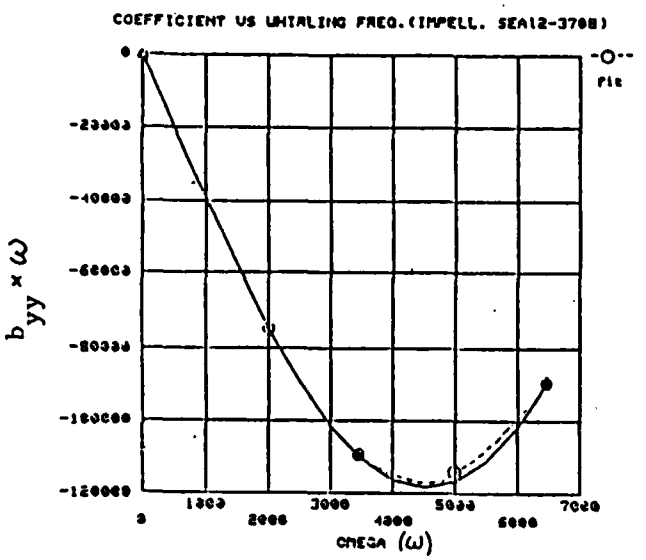

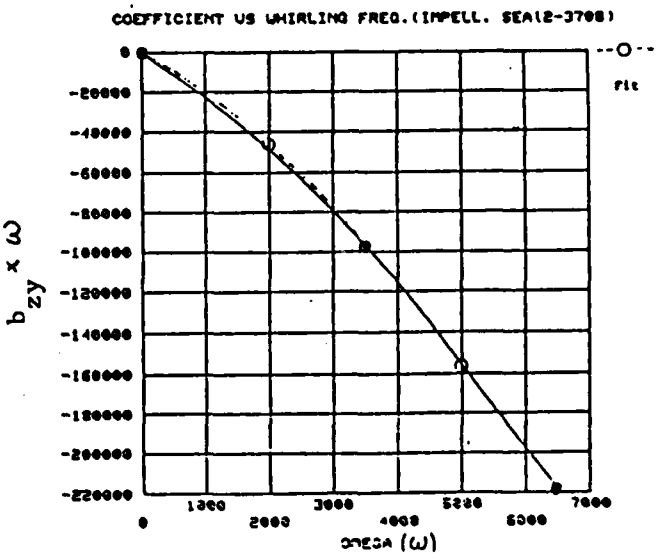

Fig. 4 2nd Impeller Seal Coefficients and their Padé Fit
(Ω = 3708 rad/sec)

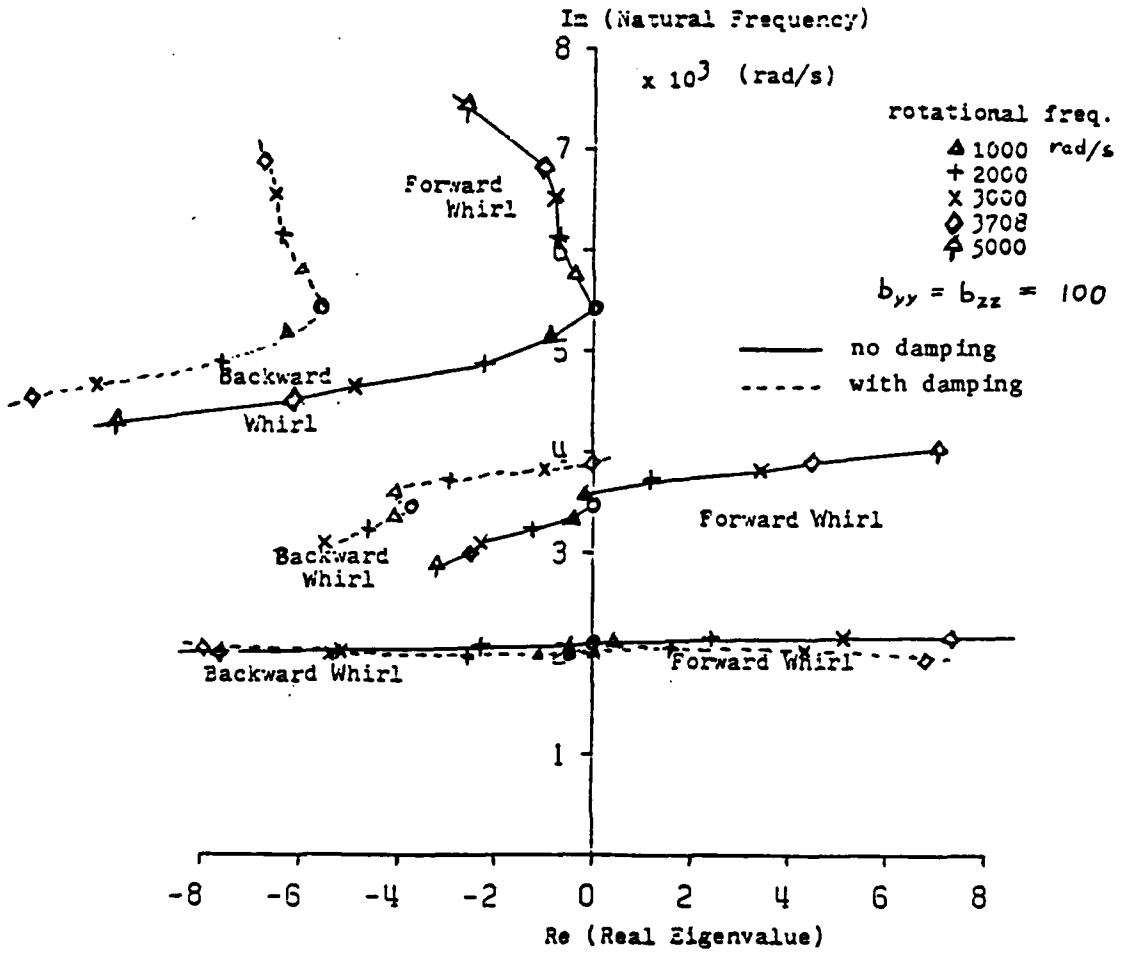

Fig. 5 Root Locus Stability Plot for Rigid Case

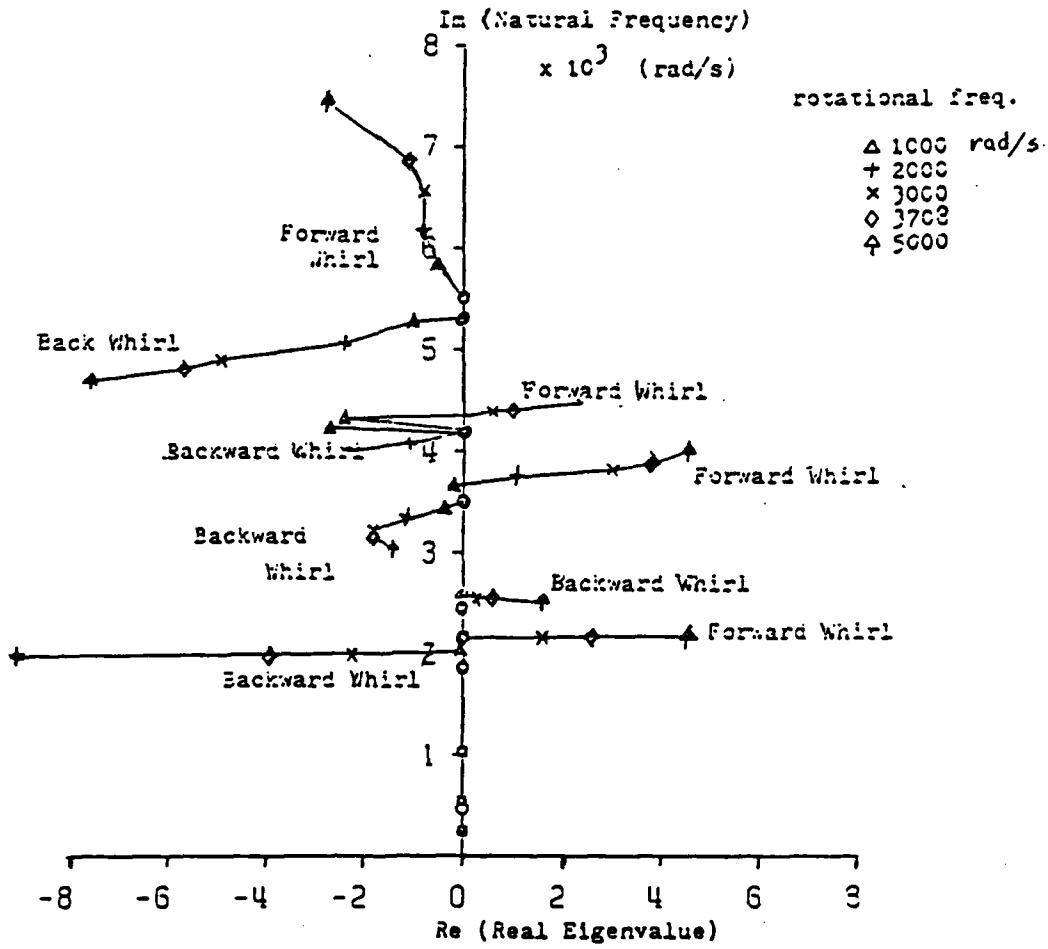

Fig. 6 Root Locus Stability Plot for Flexible Case

APPENDIX A

ANALYSIS AND PREDICTION OF FLUID FORCES IN LABYRINTH SEALS

By

Manuel Martinez-Sanchez

Otto W.K. Lee

and

Eva Czajskowski

Massachusetts Institute of Technology

Cambridge, MA 02139

(Paper submitted for publication in the ASME Journal of Engineering for Gas Tubines and Power).

ABSTRACT

A linear analytical model for the prediction of fluid forces in labyrinth seals is presented and discussed. Numerical comparisons to literature data on the important corss-stiffness k_{yx} shows agreement to within 20%. Two dominant fluid effects are identified: (a) Unsymmetric tangential momentum addition to each chamber when the flow swirl varies axially in the presence of shaft offset, and (b) Azimuthal variations of flow area within each chamber due to the offset. Both of these induce pressure nonuniformities that integrate to yield cross-forces. The direct contribution of shear forces is shown to be small, but friction does play an important role in generating the swirl changes that lead to effect (a) above. The Alford passage-contraction effect is shown to contribute only to direct stiffness, K_{xx}.

1. Introduction

Fluid-dynamic forces arising from nonuniform pressure patterns in labyrinth seal glands are known to be potentially destabilizing in high power turbomachinery. A well documented case in point is that of the space Shuttle Main Engine turbopumps (ref. 1), and other examples can be found in the literature, as for instance in the reviews of Ehrich (ref. 2) and Childs and Ehrich (ref. 3). Seal forces are also an important factor for the stability of shrouded turbines, acting in that case in conjunction with the effects of blade-tip clearance variations (ref. 4,5,6).

The basic mechanisms which produce the uneven pressure distrubtion in a labyrinth have been qualitatively or semi-qualitatively discussed in many early references (Ref. 7, for instance). In most instances, the basic agent is found to be flow swirl in the glands, either from pre-swirl (as in the case of turbine shrouds) or from frictional interaction with the rotating shaft (as in multichamber jet engine seals). Quantitative modeling of these forces has also been reported by a number of authors (refs. 8, 9, 10), using lumped-parameter models for each gland. These models yield in general predictions of the direct and cross-wise stiffnesses and damping coefficients for small shaft displacements, and are useful for linear stability analyses. Non-linear predictions for fully developed unstable operation are less advanced.

Fairly extensive data also exist on the stiffness factors of seals of various geometries (refs. 4, 5, 11, 12, 13). These have been

generally obtained in rotary rigs with adjustable shaft eccentricity. Much less satisfactory is the situation with respect to data on damping coefficients due to labyrinth seals, since these require dynamic measurements on either vibrating shafts, or shafts fitted with adjustable whirl mechanisms. Yet these data are almost as essential as those on stiffnesses, since the corresponding induced forces are of the same order. Ref. (13) reports damping data for a labyrinth, but with no positive control or measurement of inlet whirl.

In this paper we report on the development of a linear model for the prediction of labyrinth seal forces and on its comparison to available stiffness data. We also present a discussion of the relevance of various physical effects that lead to fluid forces on the labyrinth.

2. Model Formulation

The model is very similar in its main outline to those of Kostyuk (ref. 8) and Iwatsubo (ref. 9). It describes the flow of an ideal gas through the seal chambers, assuming largely constant temperature, but allowing for isentropic acceleration towards the narrow gaps and also for isentropic azimuthal flow redistribution in each chamber. Each chamber is assigned a pressure P_i and azimuthal velocity c_i, and these quantities are governed by equations of mass and azimuthal momentum conservation, written in integral form.

The axial flow rate q through each seal throttling is approximated by a commonly used expression, which basically derives from Bernoulli's

equation with a density halfway between those of the two adjacent chambers. Per unit length in the azimuthal direction, this gives

$$q_i = \mu_i \delta_i \sqrt{\frac{p_{i-1}^2 - p_i^2}{R_g T}} \qquad (1)$$

where δ_i is the width of the narrow gap (see fig. 1) and $\mu_i = c_{c_i} \beta_i$ is the product of the usual contraction coefficient c_{c_i} times a carryover factor β_i to account for nonzero upstream axial velocity and nonzero pressure recovery in the downstream chamber. Eq. (1) is assumed to apply locally at each time t and azimuth ϕ. This semi-incompressible approximation is known to be reasonalbe up to gap Mach numbers of about 0.5; however, the last gap or two of a labyrinth with a high overall pressure ratio may be above that Mach number, and, in particular, the last chamber may choke. We have partially accommodated this effect by retaining Eq. (1) throughout, but replacing it by a choked-flow expression in the last chamber only if the first approximation indicated sonic or supersonic conditions there.

With reference to the geometry of fig. 1, the governing equations within each chamber are those of mass and azimuthal momentum conservation:

$$\frac{\partial}{\partial t} (\rho_i f_i) + \frac{\partial}{\partial w} (\rho_i f_i c_i) + q_{i+1} - q_i = 0 \qquad (2)$$

$$\frac{\partial}{\partial t} (\rho_i f_i c_i) + \frac{\partial}{\partial w} (\rho_i f_i c_i^2) + q_{i+1} c_i - q_i c_{i-1} + \tau_i \text{"U"} - \tau_i \text{"U"}$$

$$+ f_i \frac{\partial P_i}{\partial w} = 0 \qquad (3)$$

These equations are first linearized about a condition of zero eccentricity. The zero'th order approximation provides a basic flow rate q^* and pressure and azimuthal velocity distributions P_i^*, c_i^*, (Appendix 1). The first approximation then provides linear equations for the perturbations, defined by

$$p_i = p_i^* (1 + \xi_i) \; ; \; q_i = q_i^* (1 + \zeta_i) \; ; \; c_i = c_i^* (1 + \eta_i) \qquad (4)$$

where ξ_i, ζ_i, η_i are functions of t and $w = R_s \phi$. The right hand sides of these equations are determined by an assumed accentric motion of the shaft, whose center follows a circular path

$$x_c + iy_c = r\, e^{i\Omega t} \qquad (5)$$

where Ω is the shaft vibration frequency, closely identified with one of its natural frequencies. This results in a gap distribution (see Fig. 2)

$$\delta_i = \delta_i^* - r \cos(\phi - \Omega t) \qquad (6)$$

where $\phi - \Omega t$ is the angle measured in the whirl direction from the narrowest gap. The perturbation quantities ξ_i, η_i and ζ_i then have similar sinusoidal variations in time and space, with whirl-dependent

amplitudes and phases:

$$\xi_i = \mathrm{Re}[\hat{\xi}_i e^{-i(\phi-\Omega t)}], \text{ etc} \tag{7}$$

where Re() indicates real part and $\hat{\xi}_i$ is a complex amplitude factor.

The process of linearizing Eqs. (1),(2) and (3) is straightforward, but tedious (see Refs. 14,15). After eliminating flow variations (ζ_i) in favor of pressure (ξ_i) and tangential velocity (η_i) variations, one obtains a system of two linear equations per labyrinth gland as follows:

$$\begin{bmatrix} iF_i & 0 \\ iQ_i & iS_i \end{bmatrix} \begin{Bmatrix} \hat{\xi}_{i-1} \\ \hat{\eta}_{i-1} \end{Bmatrix} + \begin{bmatrix} -B_i + \Omega A_i - iE_i & -C_i \\ -M_i + \Omega K_i - iP_i & -N_i + \Omega L_i - iR_i \end{bmatrix} \begin{Bmatrix} \hat{\xi}_i \\ \hat{\eta}_i \end{Bmatrix}$$

$$+ \begin{bmatrix} iD_i & 0 \\ iO_i & 0 \end{bmatrix} \begin{Bmatrix} \hat{\xi}_{i+1} \\ \hat{\eta}_{i+1} \end{Bmatrix} = \begin{Bmatrix} -Z_i + \Omega J_i - iG_i \\ -Y_i + \Omega X_i - W_i \end{Bmatrix} r \tag{8}$$

The expressions for the coefficients A_i, B_i ....., Z_i are given in Appendix 2. For the first chamber (I = 1), $\hat{\xi}_{i-1}$, $\hat{\eta}_{i-1}$ represent the inlet non-uniformity, and for the last chamber (i = k), they represent the outlet nonuniformity. For the calculations reported here, these were taken to be zero.

If the pressure perturbations $P_i \xi_i(\phi,t)$ are calculated for each of the gaps, then the net pressure forces are obtainable by integration around the rotor periphery, followed by summation for all chambers. It is advantageous to project the forces in the directions towards the

instantaneous minimum gap (F_d) and 90^0 ahead of it in the whirl direction (F_q), as shown in Fig. 2. We obtain for each chamber

$$F_{d_i} + F_{q_i} = -R_s \ell_i \int_0^{2\pi} P_i^* \xi_i e^{i(\phi-\Omega t)} d\phi = -\pi R_s \ell_i P_i^* \hat{\xi}_i \qquad (9)$$

The forces F_x, F_y along the fixed coordinate directions are then given simply by

$$F_{x_i} + iF_{y_i} = (F_{d_i} + iF_{q_i}) e^{i\Omega t} \qquad (10)$$

3. The Stiffness and Damping Coefficients

The most general presentation of the results of a linear theory such as ours would be plots of the direct and quadrature forces per unit whirl amplitude $\frac{F_d}{r}$, $\frac{F_q}{r}$ versus whirl speed Ω, with rotation speed ω and other variables as parameters. Polynomial approximations for $F_d(\Omega)$ and $F_q(\Omega)$ are useful in condensing this information. The results presented here have been cast in the form of a <u>linear</u> approximation in Ω, leading to the definition of <u>stiffness</u> and <u>damping</u> coefficients according to the scheme

$$\begin{cases} F_x = -K_{xx}x_C + K_{xy}y_C - C_{xx}\dot{x}_C + C_{xy}\dot{y}_C \\ F_y = -K_{xy}x_C - K_{xx}y_C - C_{xy}\dot{x}_C - C_{xx}\dot{y}_C \end{cases} \qquad (11)$$

or, equivalently, using Eqs. (5) and (10),

$$\frac{F_d + iF_q}{r} = -(K_{xx} + iK_{xy}) - i\Omega(C_{xx} + iC_{xy}) \qquad (12)$$

Since such a representation is a truncation of some more complex behavior, the K and C coefficients must be regarded as functions of Ω. However, our results indicated fairly small deviations from linearity in Ω (see Appendix 3). Also, the linear approximation may be local (tangent) or global (secant), as illustrated schematically in Fig. 3. In the results presented here, the "secant" approximation has been used:

$$K_{xx} = -\frac{F_d(\Omega) + F_d(-\Omega)}{2r} \qquad C_{xx} = \frac{F_q(\Omega) - F_q(-\Omega)}{2\Omega r}$$

$$K_{xy} = -\frac{F_q(\Omega) + F_q(-\Omega)}{2r} \qquad C_{xy} = -\frac{F_d(\Omega) - F_d(-\Omega)}{2\Omega r} \qquad (13)$$

This can be shown to be equivalent to a commonly used procedure (Refs. (8), (9), (15) in which the equations are solved for a linearly vibrating shaft, and the calculated forces are separated into those in time phase with the displacement (K's) and those at 90^0 (C's).

A very simplified dynamic model will help to put in perspective the roles of the different coefficients in stability analysis. Assuming a shaft with mass M and structural stiffness K_0, the equations of motion for small side displacements x, y can be combined into

$$M z + \hat{C} \dot{z} + \hat{K} z = 0$$

where $\hat{C} = C_{xx} + i\, C_{xy}$, $\hat{K} = K_0 + K_{xx} + i\, K_{xy}$ and $z = x + iy$.

Assuming K_{xx}, K_{xy}, $C_{xx}^2/4M$ and $C_{xy}^2/4M$ are all small compared to K_0, as is likely to be the case in practice, we can define the (small) nondimensional parameters

$$k_{ij} = \frac{K_{ij}}{K_0} \quad ; \quad \zeta_{kj} = \frac{C_{ij}}{2\sqrt{K_0 M}}$$

Then a simple analysis shows that, to the first approximation, the shaft complex displacement z will vary as $e^{\Omega_s t}$, where

$$\frac{\Omega_s}{\sqrt{K_0/M}} \simeq \left(-\zeta_{xx} \pm \frac{1}{2} k_{xy} \right) + i \left(\pm 1 \pm \frac{1}{2} k_{xx} - \zeta_{xy} \right)$$

Thus any nonzero k_{xy} will be destabilizing (in one or the other whirl direction), while a negative ζ_{xx} will be always destabilizing; k_{xx} and ζ_{xy} will simply modify the shaft natural frequency. Also, the effects of equal values of $|K_{xy}|$ and $-\Omega\, C_{xx}$ are seen to be equivalent.

This discussion has served to indicate that knowledge of the damping factor C_{xx} is at least as essential to studies of fluid-induced destabilizing forces as is the side force factor K_{xy}. Yet, due to the more difficult experimental conditions, much fewer data are available on C_{xx} than on K_{xy}.

4. Discussion of the Physical Effects Involved

4.1 Non-Dimensional Formulation

For purposes of analysis it is advantageous to recast Eqs. (8) in non-dimensional form. It is also convenient to replace the second of the two equations in (8) (i.e., the momentum equation) by the combination resulting from subtracting from it the first equation (continuity), times c_i^* .

the list of dimensionless parameters used contains a few purely geometrical ratios, namely

$$L_i = \frac{\ell_i}{R_g} \quad ; \quad \Delta_i = \frac{\delta_i^*}{h_i} \quad ; \quad H_i = \frac{h_i}{\ell_i} \quad ; \quad \epsilon_i = \frac{r}{\delta_i^*}$$

$$\alpha_i = \frac{\delta_i^*}{\delta_{i+1}^*} \qquad \beta_i = \frac{\mu_{i+1}^* \, \delta_{i+1}^*}{\mu_i \, \delta_i} \tag{14}$$

plus a number of flow-related parameters. These are:

(a) A parameter characterizing the gland-to-gland pressure ratio, or the restriction axial Mach number:

$$\tilde{q} = \frac{q^*}{\mu_i \, \delta_i^* \, \rho_i^* \sqrt{R_g \, T}} = \sqrt{\left(\frac{P_{i-1}^*}{P_i^*}\right)^2 - 1} \tag{15}$$

If M_{z_i} is the axial Mach number (defined with the chamber speed of

sound, $\sqrt{\gamma R_g T}$), in the (i-1, i) restriction, one can show that, within the model approximations,

$$\tilde{q} = \frac{\sqrt{\gamma}\ M_{z_i}}{1 - \frac{\gamma}{4} M_{z_i}^2} \tag{16}$$

(b) A parameter related to the flow swirl in each gland, or to the angle between the flow in the restriction and the axial direction:

$$\sigma_i = \frac{\rho_i^* \delta_i^* c_i^*}{q^*} = \frac{1 - \frac{\gamma}{4} M_{z_i}^2}{\gamma \mu_i} \frac{M_{t_i}}{M_{z_i}} \tag{17}$$

where M_{t_i} is the tangential Mach number, $M_{t_i} = c_i^* / \sqrt{\gamma R_g T}$

(c) A mixed parameter which compares pressure gradients to dynamic head gradients:

$$\Pi_i = \frac{P_i^* \delta_i^*}{q^* c_i^*} = \frac{1 - \frac{\gamma}{4} M_{z_i}^2}{\gamma \mu_i} \frac{1}{M_{z_i} M_{t_i}} \tag{18}$$

(d) A "flow twisting" parameter which measures the axial swirl gradients:

$$g_i = 1 - \frac{c_{i-1}^*}{c_i^*} \tag{19}$$

Finally, the spin and whirl angular velocities of the shaft are expressed by the parameters

$$s_i = \frac{\omega R_s}{c_i^*} \quad ; \quad w_i = \frac{\Omega R_s}{c_i^*} \tag{20}$$

In terms of these variables, the set of equations (8) becomes:

$$-(1 + \frac{1}{\tilde{q}^2})\,\hat{\xi}_{i-1} + [\frac{1+\beta_i^2}{\tilde{q}^2} + i\,\frac{L_i}{\Delta_i}\,\sigma_i\,(w_i - 1)]\,\hat{\xi}_i - \frac{\beta_i^2 - 1}{\tilde{q}^2}\,\hat{\xi}_{i+1} - i\,\frac{L_i}{\Delta_i}\,\sigma_i\,\hat{\eta}_i$$

$$= \epsilon_i\,[\alpha_i + i\,L_i\,\sigma_i\,(w_i - 1)] \tag{21}$$

$$g_i\,(1 + \frac{1}{\tilde{q}^2})\hat{\xi}_{i-1} + \{-\frac{g_i}{\tilde{q}^2} + \frac{\sigma_i}{\Delta_i H_i}\,\frac{\lambda_i'}{8\gamma}\,[1 - \frac{\lambda''_i\,U''_i}{\lambda'_i\,U'_i}(s_i - 1)^2] - i\Pi_i\,\frac{L_i}{\Delta_i}\}\hat{\xi}_i$$

$$-(1 - g_i)\,\hat{\eta}_{i-1} + \{1 + \frac{\sigma_i}{\Delta_i H_i}\,\frac{\lambda'_i}{4}\,[1 + \frac{\lambda''_i\,U''_i}{\lambda'_i\,U'_i}\,(s_i - 1)]$$

$$+ i\,\frac{L_i}{\Delta_i}\,\sigma_i\,(w_i - 1)\}\,\hat{\eta}_i = \epsilon_i\,g_i \tag{22}$$

In order to assess the numerical range of the various terms in these equations, it is useful to particularize to the case of a simple 1-cavity (two restrictions) seal. If the upstream and downstream fluid variables are assumed uniform, then $\hat{\xi}_{i-1} = \hat{\xi}_{i+1} = \hat{\eta}_{i-1} = 0$ in this case. In what follows we will drop the subscript i, since only the

value i=1 is involved. This case also allows a relatively simple calculation of the chamber swirl c^* (and hence of $g = 1 - \frac{c_0^*}{c^*}$): the steady-state momentum equation (Eq. A-3) gives a zeroth order solution $c^* \simeq c_0^*$ when friction is neglected. Iterating with this value then gives an improved estimate as follows:

$$g = 1 - \frac{c_0^*}{c^*} = - \frac{\lambda' \sigma_0}{8} \frac{}{H\Delta} \left[1 - \frac{\lambda'' \, U''}{\lambda' \, U'} (s_0 - 1)^2 \right] \qquad (23)$$

4.2 Orders of Magnitude and Simplified Equations

For concreteness, we will now refer to the results reported in Appendix 3 for a particular choice of parameters. We find in this case friction factors $\lambda' \sim \lambda'' \sim 0.006$, and axial and tangential Mach numbers $M_z \simeq 0.61$, $M_t \simeq 0.28$ (at an inlet swirl velocity $c_0^* = 100$ m/sec). This, plus the dimensions chosen, gives:

$\Delta = 0.083$ $\quad L = 0.053$ $\quad H = 0.38$ $\quad \alpha = 0$ $\quad \beta = 1$

$\tilde{q} = 0.83$ $\quad \sigma = 0.28$ $\quad \Pi = 4.4$ $\quad g = -0.025$ $\quad \omega = 0.75$

Using these values it is found that the terms involving the friction factors λ', λ'' in Eq. (22) are about an order of magnitude smaller than other competing terms, and can be neglected, with the important exception that the whole RHS of Eq. (22) is proportional to g, and hence to the friction factors (Eq. 23), and cannot a-priori be

ignored. Eqs. (21) and (22) reduce to:

$$[\frac{1+\beta^2}{\tilde{q}^2} + i\frac{L}{\Delta}\sigma(w-1)]\hat{\xi} - i\frac{L}{\Delta}\sigma\hat{\eta} \simeq \epsilon\{\alpha + iL\sigma(w-1)] \quad (24)$$

$$-i\Pi\frac{L}{\Delta}\hat{\xi} + [1 + i\frac{L}{\Delta}\sigma(w-1)]\hat{\eta} \simeq \epsilon g \quad (25)$$

This can yet be reduced by noting that $\frac{L}{\Delta}\sigma(w-1) \simeq -0.05$; if this term is dropped from the bracketed terms, we obtain:

$$\hat{\xi} = \epsilon\frac{\alpha + i\,L\sigma(w-1+g/\Delta)}{\frac{1+\beta^2}{\tilde{q}^2} + \Pi\sigma\frac{L^2}{\Delta^2}} \quad (26)$$

$$\hat{\eta} \simeq \epsilon\frac{\frac{1+\beta^2}{\tilde{q}^2}g - \Pi\sigma\frac{L^2}{\Delta}(w-1) + i\alpha\Pi\frac{L}{\Delta}}{\frac{1+\beta^2}{\tilde{q}^2} + \Pi\sigma\frac{L^2}{\Delta^2}} \quad (27)$$

4.3 Interpretation of Physical Effects

Since $F_p + iF_q$ is proportional to $-\hat{\xi}$ (Eq. 9), we see from Eq. (26) that the "passage contraction factor", α, (Eq. 13) can only contribute to F_d, which is dynamically much less significant than the cross-force F_q. This result is to be contrasted with the simplified model postulated originally by Alford (Ref. 7), where axial decrease of flow gaps was identified as a major source of turbomachine whirl. The explanation is to be found in the rapid pressure redistribution by sound waves within a chamber, which makes M_z and $\tilde{q}_s$ relatively small

and prevents the second term in the coefficient of $\hat{\xi}$ in Eq. (24) from contributing a significant imaginary part to $\hat{\xi}$ due to a nonzero α. This conclusion would, of course, be reversed for cases where $\frac{\Delta}{L} = \frac{R_s \delta}{\ell h}$ is much less than taken in our example. Notice also that, within the approximations adopted, this "Alford seal effect" is the only contributor to direct (displacement-aligned) forces, and hence to seal stiffness. Other contributions would arise from terms neglected in arriving at Eqs. (24) and (25), but it is clear from this discussion that such effects are numerically smaller than those leading to cross-forces.

Concentrating now on F_q, we can use Eqs. (17) and (18) for σ and Π and substitute the imaginary part of Eq. (26) into Eq. (9), to obtain

$$F_q = \pi R_s \ell P^*_\epsilon \frac{L}{\mu} \frac{M_t M_r}{1 - \frac{\gamma}{4} M_r^2} \frac{1 - w - g/\Delta}{(1 + \beta^2) + \frac{L^2}{\Delta^2 \mu^2 \gamma}} \qquad (28)$$

The factor $1 - w - g/\Delta$ in Eq. (28) identifies the two main driving mechanisms for cross-force generation. the part $1 - w$ can be traced to the rate of change of tangential flow area, as seen by the swirling flow, and it becomes zero when $w = 1$, i.e., when $\Omega R_s = c^*$. This Ω dependence constitutes the <u>damping</u> component (C_{rr}) of the cross-force. The other part, g/Δ, is proportional to the change in swirl from inlet to chamber; this is an "ejector pump" effect, and will be discussed further in what follows. Numerically speaking, in our example, we have $1 - w = 0.25$ and $g/\Delta = -0.30$, so both these effects contribute about

equally. In terms of direction, we notice that the area-change term $1 - w$ contributes a whirling force in the direction of the flow swirl c^* whenever $\Omega < c^*/R_s$, while the term $-g/\Delta$ gives a force in the whirl direction ($F_q > 0$) whenever the flow swirl is highest (in the same sense as the whirl) at entrance, and tends to be reduced by friction.

Looking at the denominator of Eq. (28), we see that the term $1 + \beta^2$ is about five times the other part ($L^2/\Delta^2\mu^2\tau$). It can be shown that neglecting this latter term is tantamount to neglecting $-i\Pi \frac{L}{\Delta} \hat{\xi}$ in Eq. (25). Since this term arises from the azimuthal pressure gradient in the momentum equation, this shows that the unsymmetric injection of excess momentum (represented by the right hand side of Eq. (25) results mostly in an uneven azimuthal velocity ($\hat{\eta}$), with a smaller effect on azimuthal pressure redistribution ($\hat{\xi}$).

Interpretation of the dominant effects is facilitated by restoring the simplified Eqs. (24) and (25) to the original, physical variables. Using primed symbols to represent the fluctuating parts of quantities, we obtain

$$\rho^* c^* \left(\frac{\partial f'}{\partial t} + c^* \frac{\partial f'}{\partial w}\right) + \rho^* f^* \frac{\partial c'}{\partial w} + q'_{exit} - q' = 0 \qquad (29)$$

$$q^*(c' - c'_0) + (c^* - c_0)\, q'_\delta + f^* \frac{\partial p'}{\partial w} = 0 \qquad (30)$$

where q'_δ is that part of the inflow variation which is proportional to gap variation (the other part is due to the variations of cavity

pressure, and plays a smaller role in the momentum equation). If in this momentum equation (Eq. (30)) we ignore $f^* \frac{\partial p'}{\partial w}$, we obtain simply the statement that the quantity $q(c - c_0)$ remains azimuthally uniform despite the shaft eccentricity. This means that in places where more fluid is entering the cavity ($q' > 0$), its velocity increase $c - c_0$ gets reduced, so that no significant inertia force variation arises; to the extent that this balance is not achieved, (particularly when Δ/L or M_z are small) azimuthal pressure gradients also arise. The seal is in some sense acting as an azimuthal ejector pump, where variations of tangential momentum addition result in a combination of flow speed and pressure gradients.

With c' mainly determined from this momentum balance, Eq. (29) then indicates that the gradients of these velocity fluctuations, plus those of the flow area (f'), imply local net mass inflow or outflow ($q'_{exit} - q'$). As noted before, these have two parts, one proportional to $\delta'_{exit} - \delta'$, which leads to the Alford seal effect, and the other due to pressure variations: if p' is locally positive, this acts both to inhibit inflow and increase outflow, giving a net negative inflow fluctuation. It is this pressure fluctuation that eventually produces the bulk of the cross-force F_q. Note also the origin of the damping component: the material derivative of flow area $(\frac{\partial f'}{\partial t} + c^* \frac{\partial f'}{\partial w})$ vanishies if $c^* = \Omega R_s$, and generally decreases linearly as Ω increases.

4.4 Shaft Forces Due to Shear Stresses

In addition of the forces F_d and F_q discussed so far, the shear

stress fluctuations also produce net forces on the shaft. For the i^{th} chamber,

$$(F_d + iF_q)_\tau = i\, U_i'' R_s \int_0^{2\pi} \tau_i'' \ell^{i\theta} d\theta \tag{31}$$

Using our analysis, these can be expressed as

$$(F_d + iF_q)_\tau = i \frac{\lambda_i'' U''_i}{8} \rho_i^* c_i^{*2} \pi R_s (s_i - 1)[-2\hat{\eta}_i + (s_i - 1)\frac{\hat{\xi}_i}{\gamma}] \tag{32}$$

If the Alford seal effect is ignored ($\alpha = 0$), our simplified solution (Eqs. (26) and (27)) show that, for a one-cavity seal, $\hat{\xi}$ is imaginary and $\hat{\eta}$ is real (i.e., velocity fluctuations are spacially aligned with the shaft displacement, while pressure fluctuations are 90^o out of alignment). This means that only the $\hat{\eta}$ (velocity fluctuation) portion of Eq. (32) contributes to $(F_q)_\tau$. The ratio of this to the pressure-induced F_q is

$$\frac{(F_q)_\tau}{(F_q)_p} = + \frac{\lambda''}{4} (1 + 2H) M_t^2 (s - 1) \gamma \left(\frac{i\hat{\eta}}{\hat{\xi}}\right) \tag{33}$$

and, in the numerical example of App. 3, amounts to approximately 0.0015. Thus, frictional effects are secondary in directly determining cross-forces, but one should keep in mind their role in creating flow "twist", i.e., chamber-to-chamber swirl variations, which do play a significant role in the production of pressure forces.

5. Numerical Results and comparison to Literature Data

5.1 Data Used

Benckert and Wachter have published an extensive set of data (Refs. 11,16) for multichamber labyrinth seals of simple "straight" or "full" types (Fig. 4). The data were taken in a static-offset rig operating on pressureized air, and induced forces were obtained by integration of measured azimuthal pressure variations on a number of seal cavities. Labyrinths with up to 23 chambers were used. The experiments allowed variation of shaft speed, ω, overall pressure ratio P_{stn}/P_0, rotor eccentricity r, seal geometry (δ_i, ℓ_i, h_i, Fig. 1), number of chambers and entry swirl c_0^*. The seal flow rate q was measured and an averaged carryover factor μ was deduced from these data and reported in a number of instances. In our calculations we used these "measured" factors when available directly; in other cases, we adopted values measured for chambers of the same geometry, or, for the "full" type of seal, where little carryover is expected we used $\mu = 1$. In a number of separate runs, we attempted an a-priori determination of μ. The contraction coefficient c_c was taken as a function of Reynolds number and strip geometry as given by Vermes (Ref. 17), and the carry-over factor β was taken from Komotori's theory (ref. 21). The results of this procedure were unsatisfactory, with the prediction errors being several times higher than when the measured flow coefficient was used.

Data of Brown and Leong (Ref. 18) were also used for validation of the undisturbed flow predictions.

5.2 Undisturbed Flow Parameters

Figure 5 compares Brown and Leong's data on the axial pressure distribution in an 11-chamber test seal with our calculated undisturbed pressure distribution. There is good agreement except for the sharp pressure drop shown by the data between the inlet and the first chamber. This is probably a reflection of a reduced carry-over factor on the first strip; the calculation used a constant μ (the value used is irrelevant to the comparison).

Benckert and Wachter reported for one particular case the axial variation of azimuthal velocities c_i^*. This was for a 23-chamber seal with c_i^* = 40 m/sec, P_s/P_0 = .66, R_s = 0.15m, ω = 1000 rad/sec, r_i = 0.25 mm, r_2 = 0, δ^* = 0.5 mm, ℓ_i = 4 mm and h_i = 6 mm. The data are shown in figure 6, together with the code predictions. The good agreement shown is important for the prediction of disturbance side forces, which depend critically on swirl velocities. These results appear to validate the formulation used for the friction factors between the fluid and the stator and rotor surfaces (turbulent pipe flow formulae with a standard correction for "pipe" curvature)

5.3 Stiffness Coefficients Without Shaft Rotation

The cross-spring coefficients $K_{yz} = -K_{zy}$ for a number of cases from Benckert and Wachter's tests with a non-rotating shaft were

calculated and the results are summarized in Table 2 and figure 7. The key in Table 2 describing the test parameters is explained in Table 1.

The eccentricity r_i used in the tests was 0.15 mm, except for Run 17, which had r_i = 0.25 mm.

Table 1 Key for Table 2 (2nd column)

(Type, h, δ, ℓ)

Type	h: chamber height	δ: clearance	ℓ: pitch
S = Straight-through	0 = 2.75mm	0 = 0.25mm	0 = 5mm
F = Full-interlocking	1 = 6.25mm	2 = 0.5mm	1 = 8mm
	3 = 6mm		2 = 4mm

As Figure 7 illustrates, the calculated values are somewhat lower than the data (about 19% for series (s,0,0,0), 5% only for series (s,1,0,0)). The trends of the calculation are in agreement with those observed in the tests. In particular, K_{yz} is seen in figure 8 to be approximately proportional to inlet swirl and to overall pressure ratio, both in the tests and in the calculations (although, as mentioned, with a somewhat lower proportionality factor in the latter case).

5.4 Stiffness Coefficients with Shaft Rotation

Results similar to those in the previous section, but including various shaft speeds are given in Table 3 and figure 9. The

eccentricity is still static (no whirl, $\Omega = 0$), and is 0.25 mm in all cases. The parameter E_0^* was used in Ref. 11 to correlate entry swirl, and is

$$E_0^* = \frac{\frac{1}{2}\rho_0 (c_0^*)^2}{p_0 + \frac{1}{2}\rho_0 V_{ax,0}^2 - p_s} \; ; \; V_{ax,0} = \frac{q^*}{\rho_0 \delta_1^*} \qquad (17)$$

The comparison of data and theory shown in figure 9 indicates more scatter, but less systematic deviation than in the cases without shaft rotation (figure 7 and 8). The agreement is best for all the cases with 17 chambers (solid symbols in figure 9), which show an average error of 8.5% and little scatter.

5.5 Discussion

The two principal sources of uncertainty in calculations of the type reported here are the friction factors (λ', λ'') and the carry-over coefficient β. The friction factor could in principle be substantially increased by the relative rotation of shaft and casing, since the fluid in each chamber is strongly sheared and develops marked secondary flow patterns, leading to enhanced mixing. Examination of data[19] for the somewhat related case of turbulent pipe flow with swirl does indeed show friction increases of up to a factor of four at high swirl. An accurate prediction of wall friction under the complex flow conditions of a labyrinth gland is not possible at this time, and this is an area requiring more experimental and analytical work.

The impact of friction factor inaccuracies on calculated cross-spring coefficients could be important, although not easily generalizable. In general, the cross-forces increase with chamber swirl, and also, in part, with swirl changes from chamber to chamber (terms M_t and g/Δ in Eq. (28)). In a multi-chamber seal with excess inlet swirl, the first effect will make K_{yx} decrease as the friction factor is increased, since the additional friction will accelerate the axial decay of flow swirl. On the other hand, the changes in swirl from chamber to chamber will be increased by an increase in friction, and this effect is dominant at low friction, and especially for short seals, where c itself does not decrease much. An example of this behavior for a one-chamber seal is presented in Appendix 3, figure A2, where it can be seen that for this particular case, increasing friction would lead to <u>increases</u> in $|K_{yx}|$. The behavior typical of long seals and large friction is illustrated in figure 10, corresponding to case 1 of Table 2; here, an increase of the friction factor above the nominal value leads to a <u>reduced</u> K_{yx}, although a reduction by more than about 0.6 would lead to the same effect.

The carry-over coefficient β is clearly another source of uncertainty in the model. Unfortunately, the state of the art in a priori predictions of β is not satisfactory. A fuller discussion of this point is given in reference 24, which discusses the relationships of the older models of Vermes[17], Egli.[20], Komotori[21] to more recent models and data (Benvenuti, et al.[25], Hendricks[26]). Numerical methods for internal, turbulent and fully separated flows are not yet capable

of better than 10-20% accuracy (see Ref. 22), but full Navier-Stokes computations are now approaching the capability for modeling Reynolds numbers of the order of 10^4, as required for labyrinths. This is probably the best hope for determination of λ and β, but for dynamics studies in seals, these 3-D methods may, in any case be too laborious, and will need to be integrated with linearized, overall models of the type described here.

6. Conclusions

A linear analytical model for the prediction of fluid forces in labyrinth seals has been presented and discussed. Comparison to literature data shows agreement to within 20% for the important cross-stiffness K_{yx}. The dominant fluid effects are shown to be (a) Unsymmetric tangetial momentum addition to each chamber when flow swirl varies axially in the presence of shaft offset, and (b) Azimuthal flow area variation due to the offset. Both of these induce an unsymmetric pressure nonuniformity that integrates to yield cross-forces. The direct contribution of shear forces is seen to be small, but friction does play an important role in generating swirl changes that lead to effect (a) above. Alford's passage contraction effect is shown to contribute only to direct stiffness.

References

1. Ek, M.C., "Solution of Subsynchronous Whirl Problem in the High Pressure Hydrogen Turbomachinery of the Space Shuttle Main Engine". SAE 14th Joint Propulsion Conference, 78-1002, July 25-27, 1978.

2. Ehrich, F.F., "Identification and Avoidance of Instabilities and Self-Excited Vibrations in Rotating Machinery", ASME Paper 72-DE-21, Oct. 1979.

3. Ehrich, F.F. and Childs, D., to appear in the ASME Journal.

4. Wohlrab, R., "Experimental Determination of Gap Flow-Conditioned Forces at Turbine Stages and Their Effect on the Running Stability of Simple Rotors". NASA TM-77293, Oct. 1983 (Translated from Doctoral Thesis at the Muenchen Tech. Univ., 1975).

5. Urlichs, K., "Clearance Flow-Generated Transverse Forces at the Rotors of Turbomachines". NASA TM-77292, Oct. 1983. (Translated from Doctoral Thesis at the Muenchen Tech. Univ., 1975).

6. M. Martinez-Sanchez, E. Greitzer and Y. Qiu, "Turbine Blade-Tip Clearance Excitation Forces", Report on Contract NAS8-35018, June 1985.

7. Alford, J.S., "Protecting Turbomachinery from Self-Excited Rotor Whirl". Journal of Engineering for Power, October 1965.

8. Kostyuk, A.G., "A Theoretical Analysis of the Aerodynamics Forces in the Labyrinth Glands of Turbomachines". Teploenergetica. 1972, 19 (11), pp 29-33.

9. Iwatsubo, T., "Evaluation of Instability Forces of Labyrinth Seals in Turbines or Compressors". NASA CP 2133, May 1980.

10. Wyssmann, H.R., Pham, T.C and Jenny, R.C., "Prediction of Stiffness and Damping Coefficients for Centrifugal Compressor Labyrinth Seals". ASME Paper 84-GT-86.

11. Benckert, H. and Wachter, J., "Flow-Induced Spring Coefficients of Labyrinth Seals for Application in Rotor Dynamics:. NASA CP 2133, May 1980.

12. Wright, D.V., "Air Model Tests of Labyrinth Seal Forces on a Whirling Rotor". Journal of Engineering for Power, Trans. ASME, Vol. 100, p 533, 1978.

13. Wright, D.V., "Labyringh Seal Forces on a Whirling Rotor", ASME AMD, Vol 55, pp 19-31.

14. Celorio-Villasenor, A., "Analysis of Disturbing Aerodynamic Forces in Labyrinth Seals". MS Thesis, Dept. of Aeronautics and Astronautics, MIT, September 1982.

15. Lee, O.W.K., "Prediction of Aerodynamic Force Coefficients in Labyringh Seals". MS Thesis, Dept. of Aeronautics and Astronautics, MIT, February 1984.

16. Benckert, H., "Stromungsbedingte Fedeskennwerte in Labyrinthdichtungen". Doctoral Thesis, Univ. of Stuttgart, October 1980.

17. Vermes, G., "A fluid-Mechanics Approach to the Labyrinth Seal Leakage Problem", Journal of Basic Engineering, Tr. ASME, Series D, Vol. 82, No. 2, June 1960, pp. 265-275.

18. Leong, Y.M.M.S. and Brown, R.D., "Circumferential Pressure Distribution in a Model Labyrinth Seal, NASA CP 2250, May 1982.

19. Nissan, A.H. and Bresan, V.P., "Swirling Flow in Cylinders", A.I. Ch. E. Journal, Vol. 7, No. 4, Dec. 1961, pp 543-547.

20. Egli, A., "The Leakage of Steam Through Labyrinth Seals", Trans. ASME, Vol. 57, 1935, pp 115-122.

21. Komotori, K., "A Consideration on the Labyrinth Packing of Straight-Through Type Seals", Nihon Kikai Gakkai, Trans. J.S.M.E., Vol 23, No. 133, 1957, pp 617-623.

22. Wadia, A.R. and Booth, T.C., "Rotor Tip Leakage: Part II - Design Optimization Through Viscous Analysis and Experiment". ASME Paper 81-GT-72.

23. Adams, M.L., Mackay, E., and Diaz-Tous, I.A., "Measurement of Interstage Fluid-Annulus Dynamical Properties". NASA CP 2250, pp 147-156, May 1982.

24. Czajskowski, Eva, "Pressure Distributions Around Two-Dimensional Labyrinth Seal Chambers: Experiments and Analysis". M.S. Thesis, Dept of Aeronautics and Astronautics, MIT, August 1985.

25. Benvenuti, F., Ruggieri, G. and Tomasini, E.P., "Analytical and Experimental Development of Labyrinth Seals for Process Centrigual Compressors". ASME Spring Meeting, New Orleans, March 9-13, 1980.

26. Hendricks, R.C., "A Comparison of Flow Rates and Pressure Profiles for N Sequential Inlets and Three Related Seal Configurations", NASA TM 83442.

Appendix 1. The Unperturbed Solution

Squaring Eq. (1) and adding for all chambers yields for the nominal flow rate

$$q^* = \left[\frac{p_0^2 - p_n^2}{R_g T \sum_{i=1}^{K} \left(\frac{1}{\mu_i^2 \delta_i^{*2}} \right)} \right]^{1/2} \tag{A-1}$$

Also, adding for the first n chambers only gives

$$p_n^{*2} = p_0^{*2} - \frac{\sum_{i=1}^{n} \left(\frac{1}{\mu_i^{*2} \delta_i^{*2}} \right)}{\sum_{i=1}^{K} \left(\frac{1}{\mu_i^{*2} \delta_i^{*2}} \right)} (p_0^2 - p_s^2) \tag{A-2}$$

The momentum equation (Eq. (3)) becomes in the steady state

$$q^*(c_i^* - c_{i-1}^*) + \tau_i' U_i' - \tau_i'' U_i'' = 0 \tag{A-3}$$

with

$$\tau_i' = \frac{1}{8} \rho_i^* \lambda_i' c_i^{*2} \tag{A-4}$$

$$\tau_i'' = \frac{1}{8} \rho_i^* \lambda_i'' (\omega R_s - c_i^*)^2 \tag{A-5}$$

and λ (the Darcy friction factor) given by a modified pipe-flow expression

$$\lambda = \frac{0.3164}{R_e^{0.25}} \left[1 + 0.075\, R_e^{0.25} \left(\frac{D_h}{2R_s}\right)^{1/2}\right] \times \text{sign}\,(v_{REL}) \qquad \text{(A-6)}$$

Here R_e is the Reynolds number based on chamber height and the corresponding relative flow velocity for fixed or rotating surfaces. The factor sign (v_{REL}) is needed to give the forces τ_i', τ_i'' ther proper direction. Thus, we append the factor sign (c_i^*) to λ' and the factor sign $(\omega R_s - c_i^*)$ to λ'', both here and in the first order calculations of Appendix 2. D_h is the gland hydraulic diameter. Eqs. (A-3) through (A-6) can be solved for the distribution c_i^* of azimuthal velocities. In particular, the asymptotic velocity (c_∞^*) follows from (A-3) when $c_i^* = c_{i-1}^*$ is assumed.

Appendix 2. Coefficients for the Perturbation Equations

Let the transverse area of a gland (fig. 1) be $f_i^* = (h_i + \delta_i^*)\ell_i^*$ in the centered position. An asterisk on any variable denotes the undisturbed (centered) condition. We obtain for Eq. (7) the following coefficients.

$$A_i = \frac{f_i^*}{\gamma} \qquad B_i = \frac{c_i^* f_i^*}{R_s \gamma} \qquad C_i = \frac{c_i^* f_i^*}{R_s}$$

$$D_i = \frac{P_{i+1}^{*2} \mu_i^2 \delta_{i+1}^{*2}}{P_i^* q^*} \qquad E_i = P_i^* \frac{\delta_{i+1}^{*2} \mu_{i+1}^2 + \delta_i^{*2} \mu_i^2}{q^*}$$

$$F_i = \frac{P_{i-1}^{*2}\,\mu_i^{*2}\,\delta_i^{*2}}{P_i^{*}\,q^{*}} \qquad G_i = \frac{q^{*}}{P_i^{*}}\left(\frac{1}{\delta_{i+1}^{*}} - \frac{1}{\delta_i^{*}}\right)r \qquad J_i = \ell_i$$

$$Z_i = \frac{c_i^{*}\,\ell_i}{R_s}$$

$$K_i = \frac{f_i^{*}}{\gamma} \qquad L_i = f_i^{*} \qquad M_i = \frac{f_i^{*}}{R_s}\left(\frac{c_i^{*}}{\gamma} + \frac{R_g T}{c_i^{*}}\right)$$

$$N_i = \frac{2c_i^{*}\,f_i}{R_s} \qquad O_i = \frac{P_{i+1}^{*2}\,\mu_{i+1}^{*2}\,\delta_{i+1}^{*2}}{P_i^{*}\,q^{*}}$$

$$P_i = \frac{P_i^{*}\mu_{i+1}^{2}\,\delta_{i+1}^{*2}}{q^{*}} + \frac{P_i^{*}c_{i-1}^{*}\,\mu_i^{2}\,\delta_i^{*2}}{c_i^{*}\,q^{*}} + \frac{U'\lambda'c_i^{*}}{8\gamma} - \frac{U''\lambda''}{8c_i^{*}\gamma}\,(\omega R_s - c_i^{*})^2$$

$$Q_i = \frac{P_{i-1}^{*2}\,c_{i-1}^{*}\,\mu_i^{2}\,\delta_i^{*2}}{P_i^{*}\,c_i^{*}\,q^{*}} \qquad R_i = \frac{q^{*}}{\rho_i^{*}} + \frac{\lambda'U'}{4}\,c_i^{*} + \frac{\lambda''U''}{4}(\omega R_s - c_i^{*})$$

$$S_i = \frac{c_{i-1}^{*}}{c_i^{*}}\,\frac{q^{*}}{\rho_i^{*}} \qquad W_i = \frac{q^{*}}{\rho_i^{*}}\left(\frac{1}{\delta_{i+1}^{*}} - \frac{c_{i-1}^{*}}{c_i^{*}}\,\frac{1}{\delta_i^{*}}\right)$$

$$X_i = \ell_i \qquad Y_i = \frac{c_i^{*}\,\ell_i}{R_s}$$

Here γ is the ratio of specific heats and R_g the gas constant.

Appendix 3. Results for a Single-Cavity Seal

Sample calculations were made for a single-chamber straight-through seal with δ = 0.25 mm., ℓ = 8 mm., h = 3mm., R_s = 15

cm., ω = 1000 rad/sec, c = 100 m/sec, P_0 = 1.5 atm, P_s = 1 atm. For a range of whirl-frequencies from Ω = 0 to Ω = 750 rad/sec, the resulting direct and quadrature forces are shown in figure A-1. The quadrature force F_q, which is the one of importance for stability considerations, is seen to be very nearly linear with Ω, indicating no difference between the local and global definitions of the coefficients.

There is is, on the other hand, a slight curvature in the F_d line. The values calculated for Ω = 500 rad/sec are as follows:

	K_{xx} (N/m)	K_{yx} (N/m)	C_{xx} (N sec/m)	C_{yx} (N sec/m)
Local (Eqs. (15))	610	11350	+ 13.7	- 0.95
Global (Eqs. (16))	652	11480	13.98	- 1.02

For the same seal, with Ω = 0 throughout, figure A2 shows the effect of parametric variations of the friction coefficients (λ' and λ'' varied simultaneously) at various shaft rotation speeds.

Table 2. K_{yx} Calculated vs. Experimental ($\omega_{rot} = 0$)

Run #	Seal Type	K	P_a/P_o	C_{*_o} (m/s)	μ	K_{yx} Exper. (x 10^5 N/m)	K_{yx} Calcula. (x 10^5 N/m)
1	S,0,0,0	17	.66	38.4	.92	.75	.611
2	S,0,0,0	17	.32	52.9	.92	2.57	2.091
3	S,1,0,0	17	.32	68.3	1.02	1.57	1.45
4	S,1,0,0	17	.66	33.4	1.02	.27	0.274
5	S,1,0,0	17	.66	48.5	1.02	.423	0.411
6	S,1,0,0	17	.56	39.0	1.02	.457	0.410
7	S,1,0,0	17	.79	38.2	1.02	.218	0.224
8	S,0,0,0	17	.49	63.5	.92	1.89	1.586
9	S,0,0,0	17	.39	54.3	.92	2.22	1.747
10	S,0,0,0	17	.79	15.6	.92	.184	0.160
11	S,0,0,0	17	.49	64.2	.92	1.75	1.605
12	S,0,0,0	17	.49	34.5	.92	1.05	0.807
13	S,1,0,0	17	.49	82.68	1.02	.98	1.098
14	S,1,0,0	17	.49	40.78	1.02	.57	0.509
15	S,0,0,0	17	.32	38.2	.92	1.9	1.431
16	S,0,0,0	17	.32	27.6	.92	1.2	0.937
17	F,3,2,1	9	.49	144.7	.665	1.47	1.606
18	S,0,0,0	17	.32	45.5	.92	2.39	1.757

Average error (in absolute value) = 18.3%

(4.5% for (S,1,0,0) , 18.6% for (S,0,0,0)).

Table 3. K_{yx} Calculated vs. Experimental ($\omega_{rot} \neq 0$)

Run #	Seal Type	K	P_a/P_o	C_{*_o} (m/s)	ω_{rot} (rad/s)	μ	K_{yx} Exper. (x 10^5 N/m)	K_{yx} Calcula. (x 10^5 N/m)
1	F,3,2,2	17	.66	43.2	1000	.66	.189	0.177
2	F,3,2,2	23	.66	47.1	1000	.66	.44	0.349
3	F,3,2,2	23	.66	40.	1000	.66	.38	0.315
4	F,3,2,2	23	.79	---	993.3	.66	.307	---
5	F,3,2,2	23	.793	66.2	993.3	.66	.323	0.399
6	F,3,2,2	23	.793	49.8	746.67	.66	.189	0.228
7	F,3,2,2	17	.793	50.7	993.3	.66	.248	0.230
8	F,3,2,2	23	.657	86.74	993.3	.553[1]	.442	0.398
9	F,3,2,2	23	.657	83.64	746.67	.606[1]	.290	0.340
10	F,3,2,2	17	.66	27.9	1000	.66	.112	0.088
11[2]	F,3,2,2	17	.66	43.2	1000	.66	.20	0.187
12[2]	F,3,2,2	17	.66	27.9	746.67	.66	.12	0.0849
13[2]	F,3,2,2	17	.66	15.5	500.	.66	.044	0.0178
14[3]	F,3,2,2	23	.66	47.1	1000	.66	.40	0.328
15[3]	F,3,2,2	23	.66	30.	746.67	.66	.23	0.170
16[3]	F,3,2,2	23	.66	54.7	500	.66	.09	0.123

1 -- μ calculated from measured mass flow rate: friction factor for a channel used.
2 -- resultant forces from chambers 7 - 17 only.
3 -- resultant forces from chamoers 7 - 23 only.

Average error (in absolute value) = 23.0%

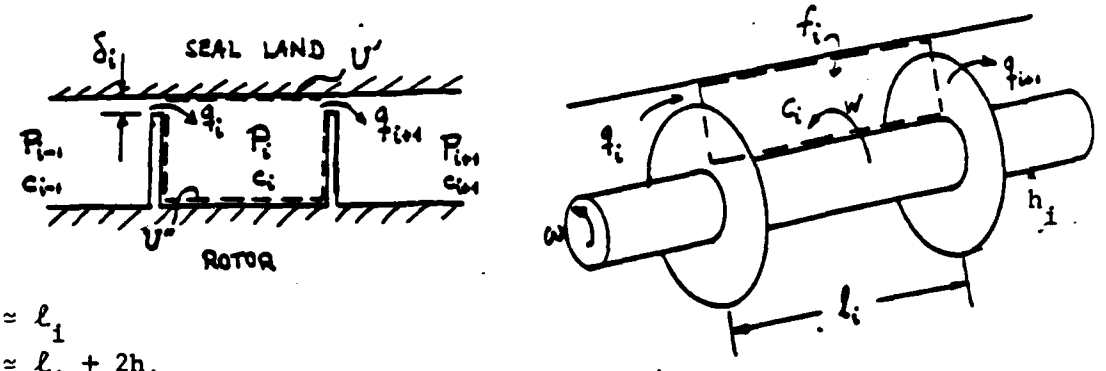

$U' \simeq \ell_i$

$U'' \simeq \ell_i + 2h_i$

Fig. 1 Geometry for labyrinth seal analysis

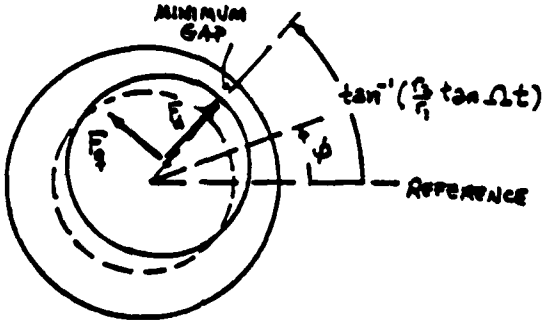

Fig. 2 Direct (F_p) and quadrature (F_q) forces due to rotor eccentricity

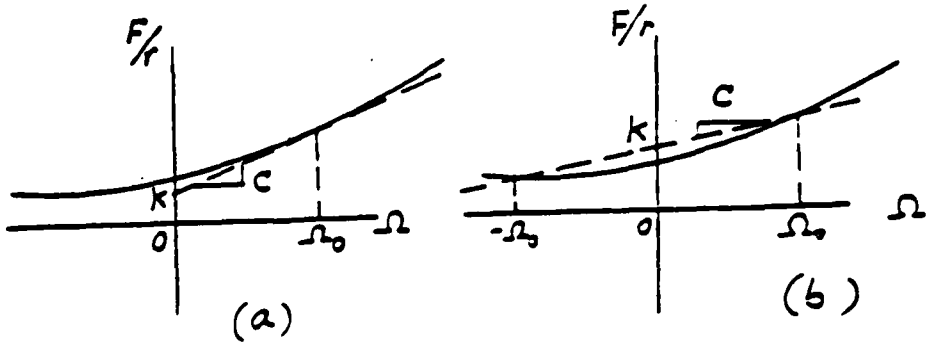

Fig. 3 Two different definitions of spring and damping coefficients.
(a) Local, (b) Global

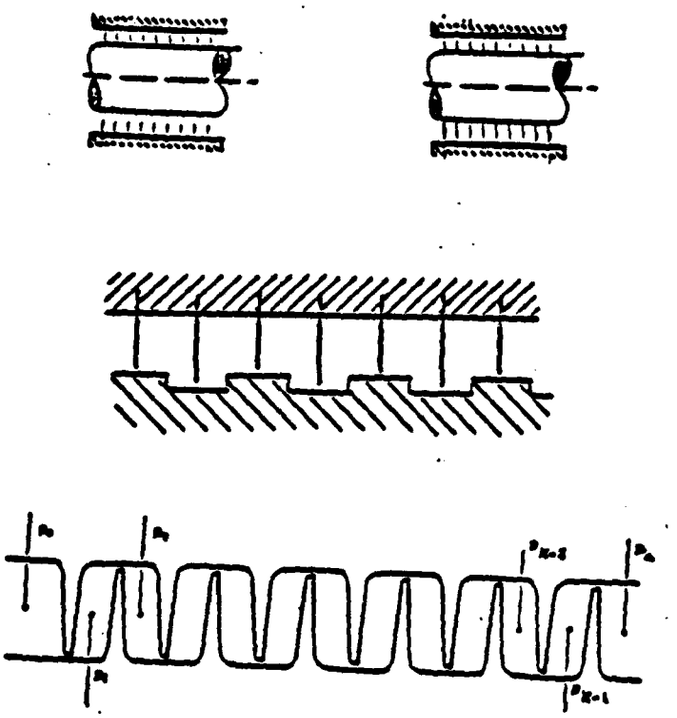

Fig. 4 Straight-through Stepped and Full Labyrinth Seals.

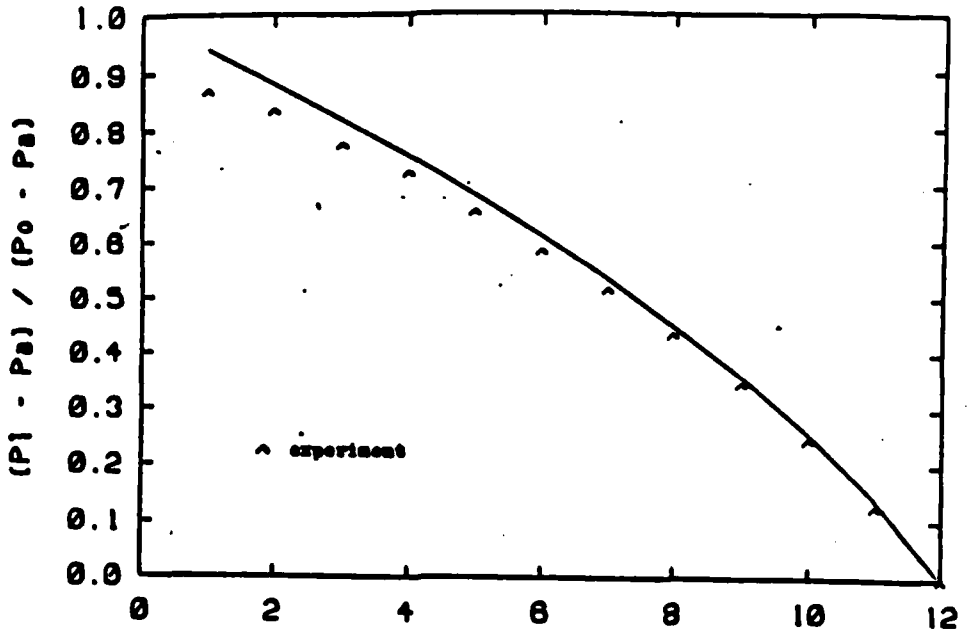

CHAMBER NUMBER 1

Fig. 5 Calculated vs. experimental axial pressure distribution

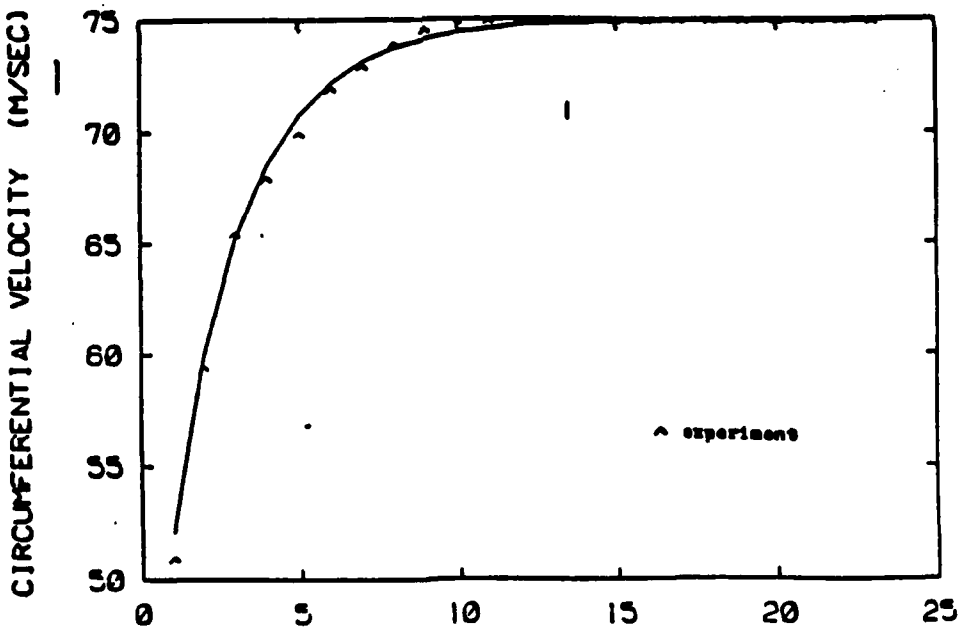

CHAMBER NUMBER 1

Fig. 6 Calculated vs. experimental circumferential velocity distribution

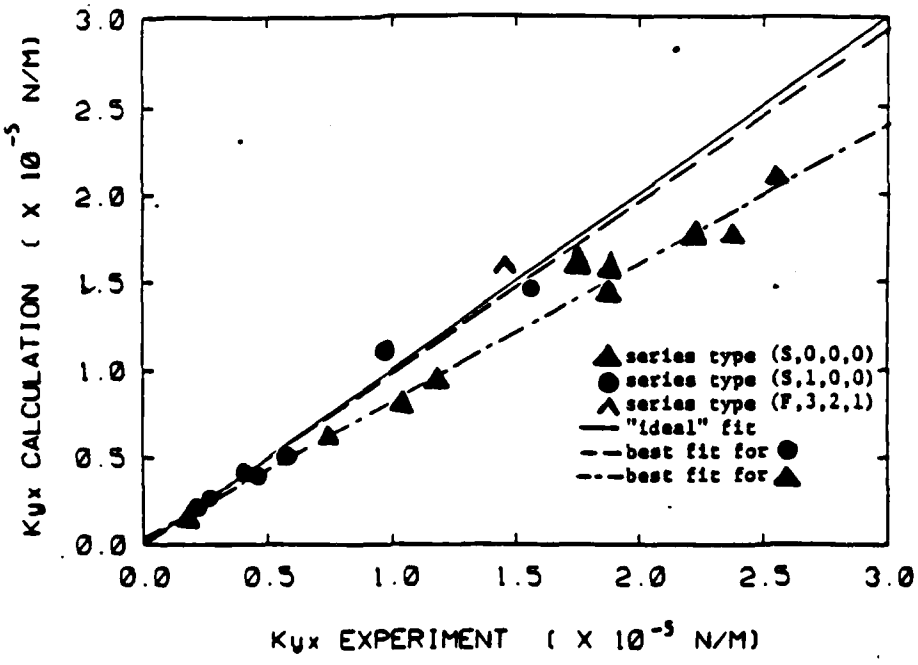

Fig. 7 Calculated vs. experimental cross spring coefficient Kyx (ω_{rot} = 0)

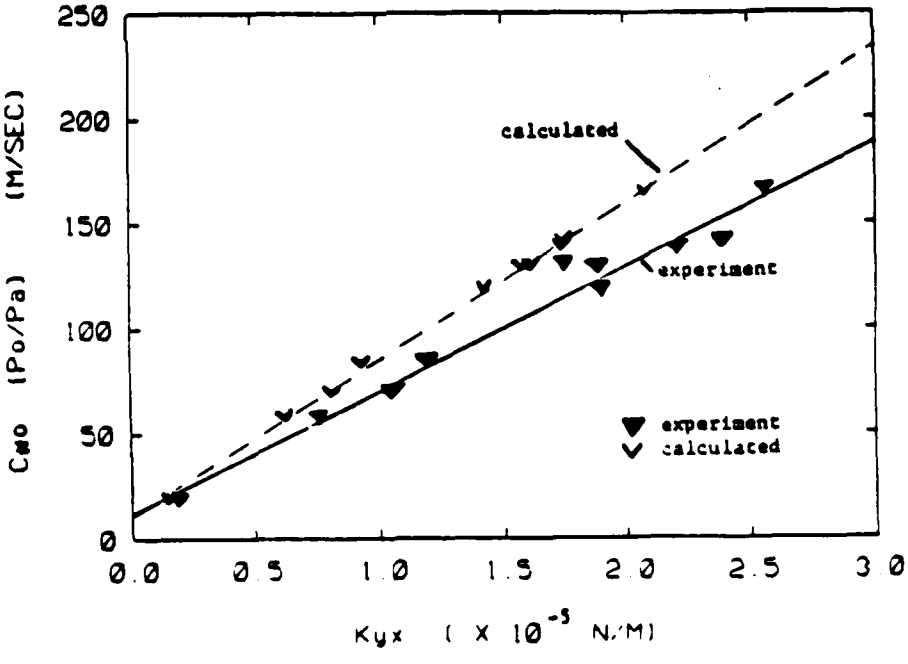

Fig. 8 Entry swirl parameter and calculated and experimental cross spring coefficient Kyx

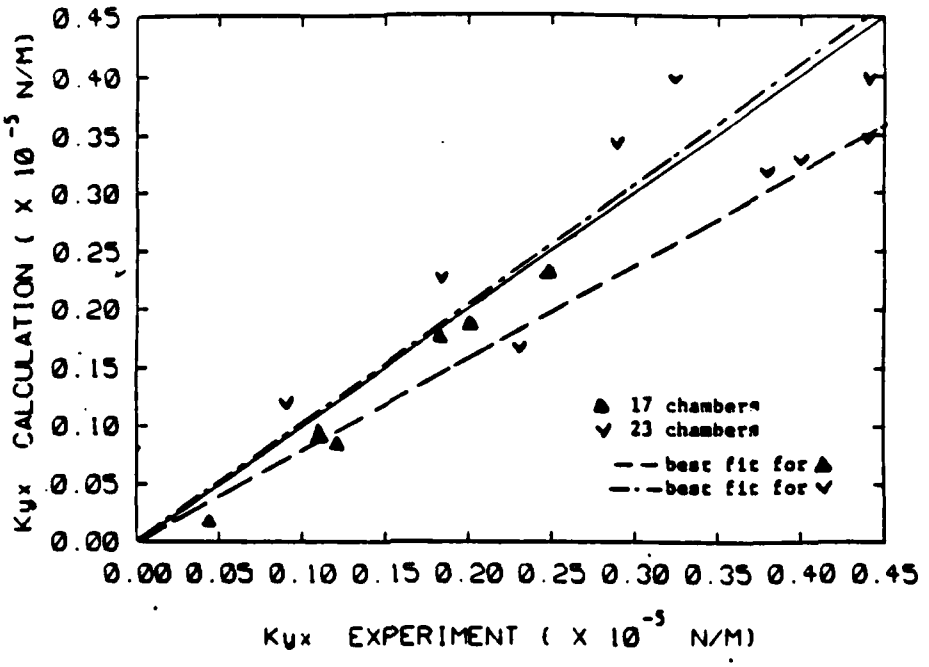

Fig. 9 Calculated vs. experimental cross spring coefficient Kyx ($\omega_{rot} \neq 0$)

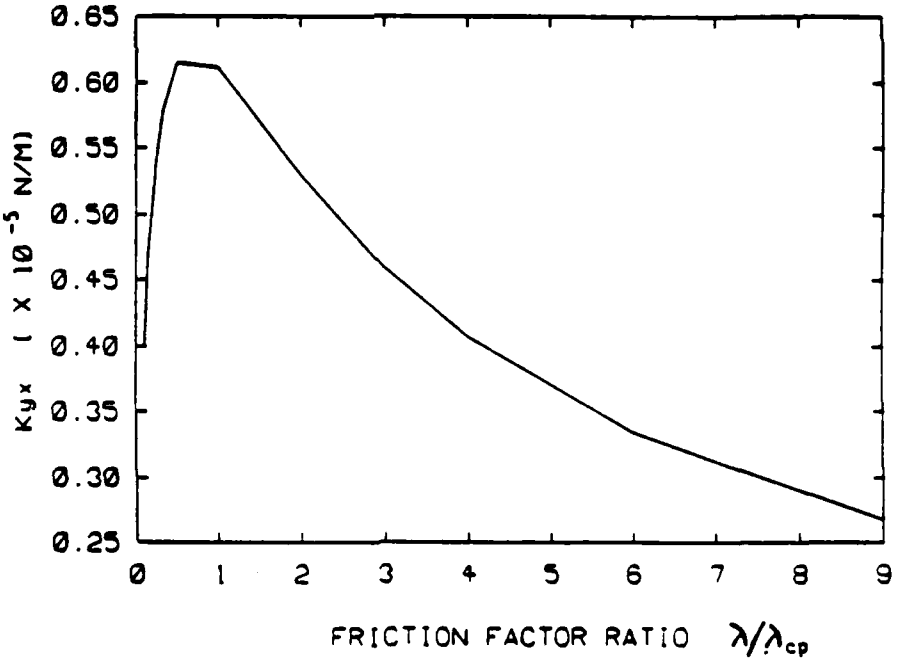

Fig. 10 Effect of friction factor on cross spring coefficient Kyx

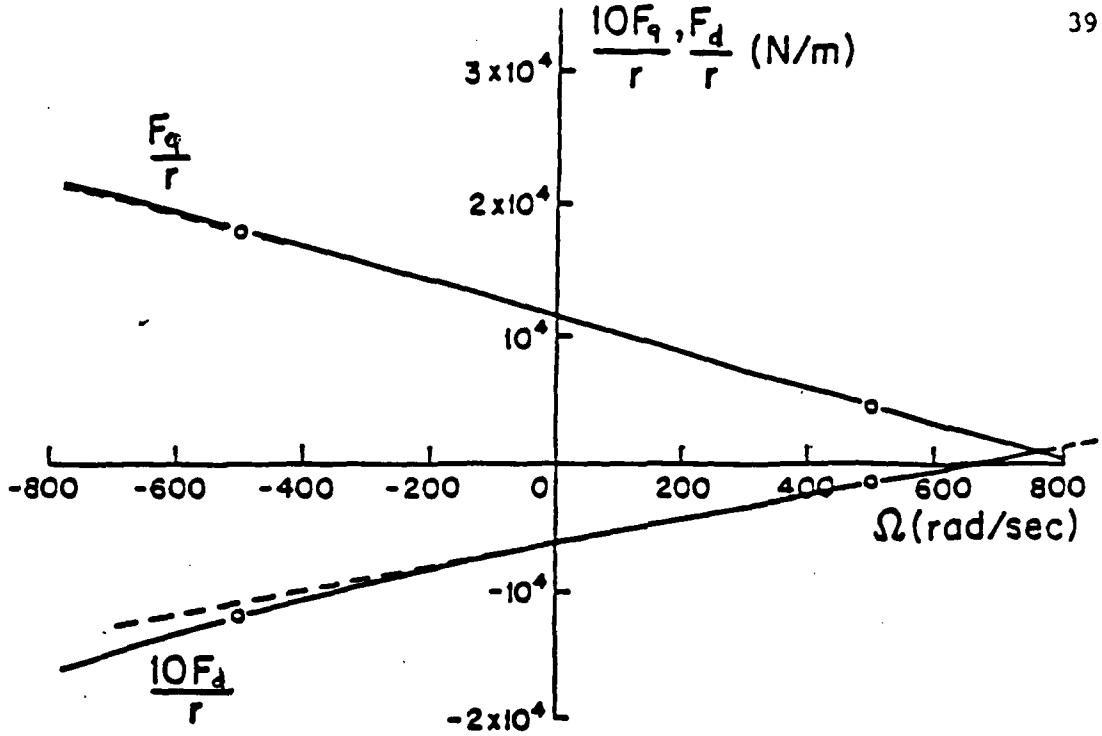

Fig. A-1 Direct and Quadrature Forces in a Short Seal

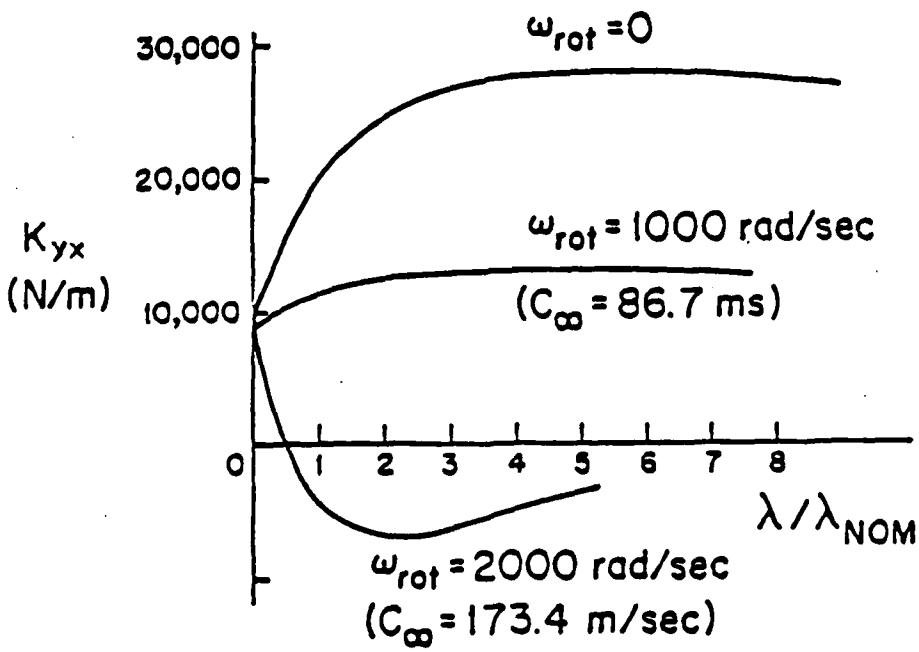

Fig. A-2 Effect of Friction Factor Variation on Cross-Stiffness in a Short Seal. Inlet Swirl Velocity C_o = 100 m/sec.

END

1-87

DTIC